

Signatures of Atmospheric Mass Loss and Planet Migration in the Time Evolution of Short-Period Transiting Exoplanets

RACHEL B. FERNANDES,^{1,2,*} GALEN J. BERGSTEN,³ GIJS D. MULDER,⁴ ILARIA PASCUCCI,³
KEVIN K. HARDEGREE-ULLMAN,⁵ STEVEN GIACALONE,^{6,†} JESSIE L. CHRISTIANSEN,⁷ JAMES G. ROGERS,⁸
AKASH GUPTA,^{9,10,‡} REBEKAH I. DAWSON,^{1,2} TOMMI T. KOSKINEN,³ KIERSTEN M. BOLEY,^{11,§} JASON L. CURTIS,¹²
KATIA CUNHA,^{13,14} ERIC E. MAMAJEK,^{15,16} SABINA SAGYNBAYEVA,¹⁷ SAKHEE S. BHURE,¹⁸ DAVID R. CIARDI,¹⁹
PREETHI R. KARPOOR,²⁰ KYLE A. PEARSON,¹⁵ JON K. ZINK,^{21,¶} AND GREGORY A. FEIDEN²²

¹*Department of Astronomy and Astrophysics, Penn State University, 525 Davey Laboratory, 251 Pollock Road, University Park, PA, 16802, USA*

²*Center for Exoplanets and Habitable Worlds, Penn State University, 525 Davey Laboratory, 251 Pollock Road, University Park, PA, 16802, USA*

³*Lunar and Planetary Laboratory, The University of Arizona, Tucson, AZ 85721, USA*

⁴*Instituto de Astrofísica, Pontificia Universidad Católica de Chile, Av. Vicuña Mackenna 4860, 7820436 Macul, Santiago, Chile*

⁵*Steward Observatory, The University of Arizona, Tucson, AZ 85721, USA*

⁶*Department of Astronomy, California Institute of Technology, Pasadena, CA 91125, USA*

⁷*NASA Exoplanet Science Institute, IPAC, MS 100-22, Caltech, 1200 E. California Blvd, Pasadena, CA 91125*

⁸*Institute of Astronomy, University of Cambridge, Madingley Road, Cambridge CB3 0HA, United Kingdom*

⁹*Department of Astrophysical Sciences, Princeton University, Princeton, NJ 08544, USA*

¹⁰*Department of Geosciences, Princeton University, Princeton, NJ 08544, USA*

¹¹*Earth and Planets Laboratory, Carnegie Institution for Science, 5241 Broad Branch Road, NW, Washington, DC 20015, USA*

¹²*Department of Astronomy, Columbia University, 550 West 120th Street, New York, NY 10027, USA*

¹³*Steward Observatory, University of Arizona, 933 North Cherry Avenue, Tucson, AZ 85721-0065, USA*

¹⁴*Observatório Nacional/MCTIC, R. Gen. José Cristino, 77, 20921-400, Rio de Janeiro, Brazil*

¹⁵*Jet Propulsion Laboratory, California Institute of Technology, 4800 Oak Grove Drive, Pasadena, CA 91109, USA*

¹⁶*Department of Physics and Astronomy, University of Rochester, Rochester, NY 14627-0171, USA*

¹⁷*Department of Physics and Astronomy, Stony Brook University, Stony Brook, NY 11794 USA*

¹⁸*Centre for Astrophysics, University of Southern Queensland, Toowoomba, QLD, 4350, Australia*

¹⁹*NASA Exoplanet Science Institute, IPAC, California Institute of Technology, Pasadena, CA 91125 USA*

²⁰*Department of Astronomy & Astrophysics, UC San Diego, La Jolla, CA, USA*

²¹*Department of Astronomy, Caltech, 1200 E. California Blvd, Pasadena, CA 91125*

²²*Department of Physics and Astronomy, University of North Georgia, Dahlonega, GA 30597 USA*

ABSTRACT

Comparative studies of young and old exoplanet populations offer a glimpse into how planets may form and evolve with time. We present an occurrence rate study of short-period (<12 days) planets between 1.8–10 R_{\oplus} around 1374 FGK stars in nearby (200 pc) young clusters (<1 Gyr), utilizing data from the Transiting Exoplanet Survey Satellite (TESS) mission. These planets represent a population closer to their primordial state. We find that the occurrence rate of young planets is higher ($64^{+32}_{-22}\%$) compared to the Gyr-old population observed by *Kepler* ($7.98^{+0.37}_{-0.35}\%$). Dividing our sample into bins of young (10–100 Myr) and intermediate (100 Myr–1 Gyr) ages, we also find that the occurrence distribution in orbital period remains unchanged while the distribution in planet radius changes with time. Specifically, the radius distribution steepens with age, indicative of a larger planet population shrinking due to the atmospheric thermal cooling and mass loss. We also find evidence for an increase (1.9σ) in occurrence after 100 Myr, possibly due to tidal migration driving planets inside of 12 days. While evidence suggests post-disk migration and atmospheric mass loss shape the population of short-period planets, more detections of young planets are needed to improve statistical comparisons with

older planets. Detecting long-period young planets and planets $<1.8 R_{\oplus}$ will help us understand these processes better. Additionally, studying young planetary atmospheres provides insights into planet formation and the efficiency of atmospheric mass loss mechanisms on the evolution of planetary systems.

1. INTRODUCTION

Prominent features in the the Gyr-old exoplanet population that we observe today are largely sculpted by the formation, migration, and evolutionary processes that take place in the early stages of planetary system formation. Two such examples are the hot Neptune desert (Beaugé & Nesvorný 2013), and the radius valley (Fulton et al. 2017; Van Eylen et al. 2018; Martinez et al. 2019; Hardegree-Ullman et al. 2020). While the hot Neptune desert is most likely sculpted by atmospheric mass loss processes such as XUV photoevaporation (Owen & Wu 2013, 2017), Roche lobe overflow (Koskinen et al. 2022), and/or core-powered mass loss (Ginzburg et al. 2016; Gupta & Schlichting 2019; Gupta & Schlichting 2020), the origin of the radius valley is still hotly debated. It could be a product of (A) evolution in that it is created by atmospheric mass loss processes such as XUV photoevaporation and/or core-powered mass loss; (B) migration, which states that Neptune-sized planets may form farther from their host star, beyond the snow line where volatiles can condense into ice, but then migrate inward due to gravitational interactions with other planets or with the protoplanetary disk (Bourrier et al. 2023; Venturini et al. 2020; Izidoro et al. 2022); or (C) planet formation and envelope capture (Lee & Connors 2021; Perez-Becker & Chiang 2013; Izidoro et al. 2015). One way to distinguish between these scenarios is to study young planets as they provide a sample much closer in time to when planets formed. By understanding what the planet population looks like at different ages, we can place constraints on the processes that dominate their formation, migration, and evolution.

With the advent of wide-field, high-precision transit surveys such as NASA’s *Kepler* (Borucki et al. 2010), *K2* (Howell et al. 2014), and TESS (Ricker et al. 2014) missions, the study of young stars and their planets has gained significant momentum. Additionally, the Atacama Large Millimeter Array (ALMA) for high-resolution imaging of protostars and protoplane-

tary disks, along with direct imaging instruments on large optical and near-infrared telescopes, has made this research even more timely. The *K2* mission, a follow-up to the highly successful *Kepler* mission, focused on the discovery of a variety of exoplanets in the ecliptic plane. While the mission’s primary objective was not specifically to study young exoplanets, *K2* made several notable detections of young exoplanets while surveying the Pleiades, Taurus, Hyades, Praesepe and Upper Scorpius clusters (e.g., Mann et al. 2016a,b, 2017; Ciardi et al. 2018; Rizzuto et al. 2017, 2018; Gaidos et al. 2017; Vanderburg et al. 2018). Thorough investigations have already started to uncover the ways in which young planets differ from their Gyr-old counterparts. For example, Christiansen et al. (2023) studied the intermediate age (600–800 Myr) clusters Praesepe and Hyades in which planets had previously been found using data from the *K2* mission. For GKM host stars, they found a significantly elevated occurrence rate of hot (<10 day), 1.8 – $4 R_{\oplus}$ sub-Neptunes (78–109%) compared to the same parameter space for *Kepler* (16%), which targeted older field stars. This substantial difference strongly indicates that such planets are far more abundant at younger stellar ages.

However, it was not until the TESS mission that we were able to sample a wide variety of young planets across different ages. During its two-year primary mission (PM), TESS observed 26 sectors of the sky for 27 days each, covering about 85% of the sky. This was followed by a three-year extended mission (EM1). In the first year of EM1, TESS revisited the four clusters observed by *K2*, then spent the remaining two years observing the southern and northern hemispheres. Throughout PM and EM1, TESS obtained Full Frame Images (FFI) in 30-min and 10-min cadence modes, respectively, providing a relatively untapped reservoir of young planetary systems. In fact, the discovery of several young planets using TESS has revealed that the young planets are larger in size, when compared to those in the Gyr-old population (e.g., Newton et al. 2019, 2021; Rizzuto et al. 2020; Mann et al. 2020; Nardiello et al. 2020; Bouma et al. 2020). However, this could be an observational bias where the high rotational variability in the light curves of younger stars makes it difficult to recover smaller planets. Therefore, in order to truly understand this population of young planets, we need to study them in an unbiased, demographic manner.

* President’s Postdoctoral Fellow

† NSF Astronomy and Astrophysics Postdoctoral Fellow

‡ 51 Pegasi b Fellow

Future Faculty in Physical Sciences Fellow

Harry H. Hess Postdoctoral Fellow

§ NASA Sagan Fellow

¶ NASA Hubble Fellow

In [Fernandes et al. \(2022\)](#) and [Fernandes & Hardegree-Ullman et al. \(2023\)](#), we computed intrinsic occurrence rates for five clusters with known transiting planets: Tucana-Horologium Association, IC 2602, Upper Centaurus Lupus, Ursa Major, and Pisces-Eridanus. We found an intrinsic planet occurrence rate of $90\pm 37\%$ for sub-Neptunes and Neptunes ($1.8\text{--}6 R_{\oplus}$) orbiting within 12.5 days of young FGK stars, consistent with that of [Christiansen et al. \(2023\)](#), and significantly higher than *Kepler*'s Gyr-old rate of $7.98\pm 0.33\%$ in the same bin. However, it is important to note that the intrinsic planet occurrence rates in both [Fernandes & Hardegree-Ullman et al. \(2023\)](#) and [Christiansen et al. \(2023\)](#) are biased given that they studied only clusters with confirmed/candidate planets. More recently, [Vach et al. \(2024\)](#) independently analysed an unbiased volume-limited sample of 7219 young stars in co-moving groups younger than 200 Myr that were observed in TESS's first four years, searching for $2\text{--}8 R_{\oplus}$, short-period (1.6–20 days) transiting planets. They computed an occurrence rate of $22^{+8.6}_{-6.8}\%$ for sub-Neptunes ($2\text{--}4 R_{\oplus}$), and $13^{+3.9}_{-4.9}\%$ for super-Neptunes ($4\text{--}8 R_{\oplus}$), respectively, from the TESS FFI data, suggesting that short-period young planets with these radii are more abundant than their Gyr-old counterparts. It is worth highlighting that [Vach et al. \(2024\)](#) is limited to <200 Myr, and therefore we do not have an unbiased understanding of clusters at intermediate ages (up to 1 Gyr).

In this work, we bridge the gap between the young (10–100 Myr) and intermediate (100 Myr–1 Gyr) aged planetary systems. By building on the methodology established in [Fernandes et al. \(2022\)](#) and [Fernandes & Hardegree-Ullman et al. \(2023\)](#), we compute the intrinsic occurrence of short-period planets in young clusters (Section 2). In Section 3, we search for transiting young confirmed planets and planet candidates in our sample of 31 young clusters and moving groups within 200 pc. Here, we also discuss how well we recover known young transiting confirmed planets and planet candidate signals in TESS EM1 FFIs using our pipeline, `pterodactyls`. We then combine these recovered planets with our homogeneously-derived catalog of updated stellar parameters ([Fernandes & Hardegree-Ullman et al. 2023](#)) to improve upon our previous estimates of their intrinsic occurrence rate around Sun-like (FGK) stars (Section 4), and place our results into context by comparing them to planet formation, migration and evolution theories in Section 5. Finally, in Section 6, we discuss how performing a quantitative comparison with *Kepler*'s Gyr-old FGK short period population can establish how the period and radius distribution

of short-period transiting exoplanets has evolved over time, and therefore provide observational constraints on migration, and atmospheric mass loss processes that affect the evolution of planetary systems with time.

2. METHODOLOGY

In [Fernandes et al. \(2022\)](#), we created `pterodactyls` – a specialized tool curated to search and vet transiting planetary signals in the highly variable TESS light curves of young stars. We also computed preliminary occurrence rates of a test sample of five clusters with known transiting planets, at the time: Tucana-Horologium Association, IC 2602, Upper Centaurus Lupus, Ursa Major and Pisces-Eridanus. For this biased sample, we conducted injection-recovery tests to characterize our detection efficiency, and computed an intrinsic planet occurrence rate of $49\pm 20\%$ for sub-Neptunes and Neptunes ($1.8\text{--}6 R_{\oplus}$) with orbital periods less than 12.5 days, which is higher than *Kepler*'s Gyr-old occurrence rates of $7.98\pm 0.33\%$. At the time, since we did not have a uniform set of stellar parameters, we conducted our injection-recovery tests and occurrence rate calculations in orbital period- $\frac{R_p}{R_*}$ space. Since exoplanet parameters depend on the properties of their host stars, it is important to properly characterize the host stars since any systematic biases in the derivation of host star parameters can negatively impact the derivation of planetary parameters. To address this issue, in [Fernandes & Hardegree-Ullman et al. \(2023\)](#), we created a uniform catalog of photometrically-derived stellar effective temperatures, luminosities, radii, and masses for 4,876 of the young stars in our sample. With these stellar radii, we updated our injection-recovery tests to orbital period-planet radius space. This also allowed us to focus solely on the young FGK stars in our sample for a better comparison to *Kepler*'s FGK occurrence rates. As part of this refinement, we excluded M dwarfs, which tend to have lower detection efficiencies due to their faintness and higher activity levels. This resulted in a 1.5x increase in detection efficiencies for short-period sub-Neptunes/Neptunes ($1.8\text{--}6 R_{\oplus}$) compared to our analysis in [Fernandes et al. \(2022\)](#).

For this work, we expanded our search to 31 young clusters, moving groups and associations within 200 pc. Here, we use data from the TESS EM1 FFIs (10-min cadence) since most of the stars in our sample do not have 2-min cadence data. A significant advantage of EM1 data is its unique coverage of the *K2* campaigns, incorporating four young clusters (Upper Scorpius, Pleiades, Hyades, and Praesepe), facilitating the recovery of planets initially detected by *K2* using TESS.

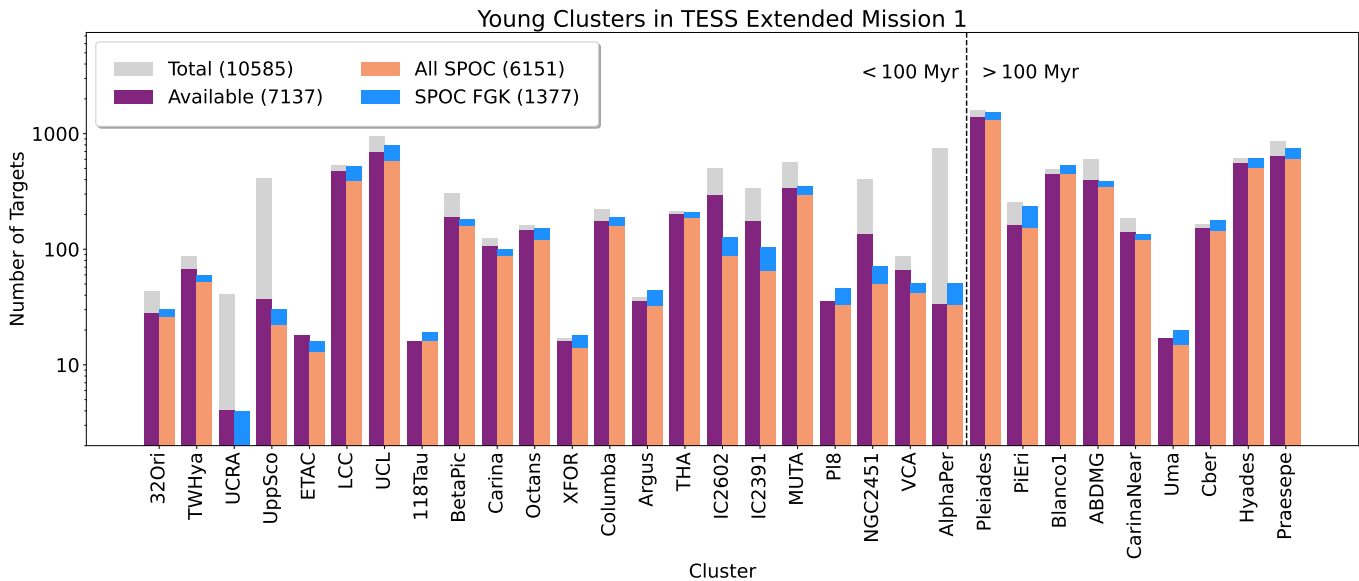


Figure 1. Bar chart showing the distribution of targets in young clusters for TESS EM1, highlighting the distinction between clusters younger than 100 Myr and those older than 100 Myr. The bars represent the total number of members in the clusters (grey dashed lines), targets observed during TESS EM1 (orange), targets that have SPOC light curves available (purple), and FGK targets for which SPOC light curves are available (blue).

2.1. Sample of Young Stellar Clusters

We assembled a sample of nearby moving groups and young clusters from the BANYAN Σ (Gagné et al. 2018) and Gaia DR2 open cluster member lists (Babusiaux et al. 2018). Additionally, we included the Argus (Zuckerman 2019), μ Tau (Gagné et al. 2020), and Pisces Eridanus (Curtis et al. 2019) groups. We restricted the distance to approximately ~ 200 pc, as Sun-like stars (particularly fainter K dwarfs) beyond this range are too faint for TESS planet detection, i.e., Neptunes can no longer be detected above the noise in the TESS light curves. Stars in clusters younger than 10 Myr were excluded due to potential disk retention (e.g., Ercolano & Pascucci 2017) and their intricate, variable light curves (e.g., Cody et al. 2014). Clusters older than ~ 1 Gyr were also omitted as most of the atmospheric mass loss is expected to have occurred within this timescale (Owen & Schlichting 2024; Rogers et al. 2024). With these criteria, we initially identified 10,585 young stars across 31 young clusters and moving groups.

2.2. pterodactyls

In our previous works (Fernandes et al. 2022; Fernandes & Hardegree-Ullman et al. 2023), we employed PSF light curves extracted using *eleanor* (Feinstein et al. 2019). For this study, we opted for the TESS SPOC FFI PDCSAP light curves from Caldwell et al. (2020) instead due to their lower RMS residual scatter compared to those from *eleanor*, enhancing our ability to detect small planets in these inherently variable light curves

(see Appendix A for more details). Of these, 7137 stars were observed during TESS EM1 (see Figure 1), and 6151 have available SPOC light curves. 5457 of the targets with SPOC light curves are usable i.e., did not have significant instrumental effects, and were searched for planet signals. After removing OBA stars, white dwarfs, late-type M dwarfs, and probable binaries as identified by Fernandes & Hardegree-Ullman et al. (2023), we were left with 2777 young stars. Because we are interested in studying the population of short-period planets around Sun-like stars (and to enable direct comparisons with *Kepler*'s Sun-like sample), we only focus on 1374 FGK-type stars for which we have homogeneously derived stellar parameters (Fernandes & Hardegree-Ullman et al. 2023).

While the TESS SPOC pipeline effectively mitigates most TESS systematics, certain instrumental effects remain in these light curves. These include mid-sector flux drops from data downlink and offsets due to errors in the uploaded Guidestar tables (see TESS' Data Release Notes for details¹). Given that these effects could create spikes in the light curve, impeding *pterodactyls*' ability to effectively detrend and detect planetary signals in our search, we refined the light curves by masking the mid-sector flux drops and adjusting offsets. We also masked several cadences that have an elevated number of transit-like detections, indicating issues with the light

¹ https://archive.stsci.edu/tess/tess_drn.html

curves in those segments (see Figures 9 and 10 in Appendix B). Following the approach in Fernandes et al. (2022), we utilized a test similar to the “Skye” metric by Thompson et al. (2018) for *Kepler* and adapted for *K2* data by Zink et al. (2020) to evaluate transit-like signals at each cadence. If the signal count exceeded 3σ , we masked those problematic cadences prior to re-running the search.

Despite transitioning from PM’s 30-min cadence *eleanor* PSF light curves to EM1’s 10-min cadence TESS SPOC light curves from FFIs, we found that the majority of the pipeline is not changed. In particular, the effectiveness of our detrending method i.e., a penalized spline optimized using rotation rate in *Wotan* (Hippke et al. 2019), planet search using *transitleastsquares* (TLS; $\text{SNR}=\text{SDE}\geq 7$), and vetting and validation tests (*EDI-Vetter Unplugged*; Zink 2019) and *triceratops* (Giacalone et al. 2021) remain unaffected. As such, no changes were made to them.

2.3. Accounting for Flux Contamination

The radii of transiting exoplanets cannot be directly measured. Instead, their value is estimated from the transit depth, which is approximately equal to the ratio between the square of the planet’s radius and the host star’s radius. However, in the case of crowded fields (typical in young cluster environments), it is highly probable that a given transit is diluted due to the light from a bound companion or a line-of-sight, unbound star. Such a dilution of the transit depth would further lead to an underestimated, and hence inaccurate, measurement of the planetary radii which in turn would affect how a planet is characterized. In fact, the dilution of the transit signal by unresolved stars in the *Kepler* field led to an underestimation of the planet radius by a factor of ~ 1.5 on average (see e.g., Ciardi et al. 2015; Teske et al. 2018).

Stellar companions, both bound and line-of-sight, decrease the ability of the pipelines to detect transits and to properly measure planetary radii. As demonstrated with the *Kepler* survey and follow-up high-resolution imagery of exoplanet candidate host stars, a proper treatment of photometric blending decreases the number of planets $\leq 2 R_{\oplus}$ by up to $\sim 20\%$ and increases the number of planets $> 6 R_{\oplus}$ by up to $\sim 68\%$ (Furlan et al. 2017). Since stars in young clusters are in close proximity to each other, there is an increased chance of photometric blending. This is even more important for TESS observations where the pixel scale is $21''$, and in the environment of stellar clusters where much of the blending is likely from other stars in the cluster that are not bound to the host star. This is of particular importance to

our work since in order to understand planetary evolution, we need a good understanding of the planet radius distribution.

However, multiplicity rates in young clusters have not been well determined in the sense that they have only been calculated for a handful of clusters (see, for e.g., Duchêne & Kraus 2013; Offner et al. 2023). Given that, we settle for a first-order approximation of the flux contamination in our clusters by using *triceratops*’s flux contamination mode (Giacalone et al. 2021) to calculate the amount of flux each star is contributing to a fixed aperture by taking into account nearby, background and line-of-sight stars from *Gaia* DR3.

3. PLANET SEARCH AND RECOVERY

In this study, we only focus on the TESS EM1 FFI (10-min cadence) data to mitigate any effects that different cadences can have on our planet recovery and demographic analyses. In our young stellar sample, there are 32 confirmed planets and planet candidates in 23 systems discovered using both the *K2* and TESS missions, out of which 28 were observed in TESS EM1 (see Table 1). We processed all of the 5457 young stellar light curves extracted from TESS EM1 FFIs through *pterodactyls*, successfully recovering 16 planets. All our recovered planets passed a Threshold Crossing Event (TCE) cut with a signal-to-noise ratio (SNR) of 7, and a signal detection efficiency (SDE) of 7. Additionally, all recovered planets passed the following statistical vetting tests in *pterodactyls*: at least two transits with data, orbital period dissimilar to the stellar rotation rate, consistency in individual transit depths, observed transit duration consistent with expected transit duration, and *EDI-Vetter*’s Individual Transit Test and Secondary Eclipse Test (Zink 2019). Finally, the phase-folded light curves of all recovered planets were validated using *triceratops* (Giacalone et al. 2021). When determining the probability of a transiting signal being an astrophysical false positive or a transiting planet, *triceratops* (by default) uses planet occurrence rate priors based on the Gyr-old exoplanet population (e.g., Howard et al. 2012; Dong & Zhu 2013; Pétigura et al. 2013; Dressing & Charbonneau 2015; Mulders et al. 2015; Mulders et al. 2018). However, the planet population around young stars is likely different from that around Gyr-old stars; for example, young planets are typically found to be larger in size. This difference can bias the probability calculations made by *triceratops*. Therefore, we also calculated the astrophysical false positive probability using non-informative (flat) priors recently implemented in *triceratops*.

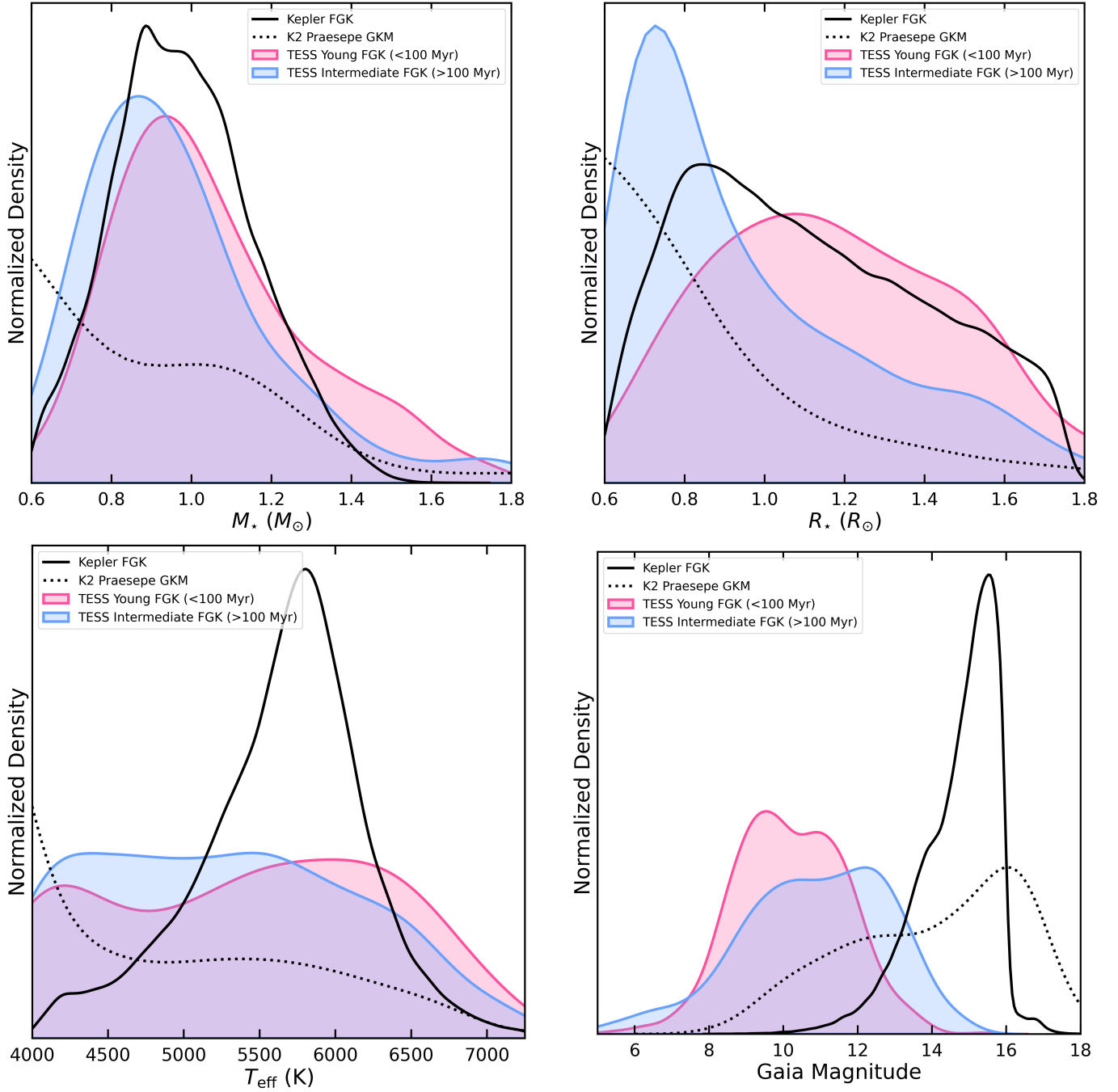


Figure 2. Normalized density distributions of stellar properties such as stellar mass (top left), radius (top right), effective temperature (bottom left), and Gaia magnitude (bottom right) for host stars from *Kepler* (black solid lines), [Christiansen et al. \(2023\)](#)'s *K2* Praesepe (black dashed lines), and TESS (pink and blue shaded regions for young and intermediate-age stars, respectively).

Out of the 12 planets we were unable to recover, 9 were *K2* discoveries that TESS was unable to recover: *K2*-136 b, c, and d, HD 283869 b, *K2*-102 b, *K2*-103 b, *K2*-104 b, and *K2*-264 b and c. This is because *K2* had better precision and a longer baseline than TESS, allowing it to detect long-period planets around fainter stars that TESS lacks the sensitivity to find. Additionally, we could not recover 3 planets (TOI 1227 b, HIP 67522 c, and AU Mic c) that were either in multi-planet systems where only one planet was recoverable due to a combination of light curve quality, and/or long period against TESS’s short baseline and small planet size.

In total, we recovered 16 confirmed planets and planet candidates, 14 of which are around Sun-like (FGK) stars, and are included in our final FGK sample of 1374 stars. However, two of these planets have orbital periods >12 days, and one planet has a radius < 1.8 R_{\oplus} . There are 4 planets in our young (10–100 Myr) age bin, and 7 planets in our intermediate (100 Myr–1 Gyr) age bin, leaving us with 11 planets that we have used in our occurrence rate calculations below. A comparison of our young and intermediate age stellar sample compared to *Kepler* and Christiansen et al. (2023)’s *K2* Praesepe sample is presented in Figure 2.

4. INTRINSIC OCCURRENCE OF YOUNG PLANETS

As can be seen in Figure 3, the unbiased radial distribution of short-period sub-Neptunes and Neptunes appears to be inflated at young (<100 Myr) ages, and to be shrinking with time. The planet sample, however, is small and it is also possible that we are only able to recover larger planets in the light curves because younger stars are more variable. Therefore, we need to carefully calculate the intrinsic occurrence rates of transiting planets in young clusters and moving groups, and compare them to that of *Kepler*, in order to verify whether young planets indeed “shrink” over time due to thermal evolution and atmospheric mass loss.

4.1. Characterizing Survey Completeness

The detection efficiency of our survey was calculated using injection-recovery tests for planets with radii of 1–10 R_{\oplus} and orbital periods of 1–14 days. For each star in our overall sample, we implemented a 3×4 injection-recovery (log-spaced) grid to balance computational efficiency with robust sampling of the parameter space. We interpolated results to a finer grid, achieving a higher-resolution detectability map for small variations in planetary properties. However, to better sample the detection efficiency for FGK stars, we performed injections on a finer 9×9 grid (81 injections per star), randomly drawing the P/R of each injection from uniform distributions

within each grid cell. We also allowed the impact parameter b to vary between 0 and 0.9 for each injection. Because b is derived from the inclination, thus requiring a measure of stellar radius which we only derived for FGK stars, we assumed $b=0$ (central transit) while measuring the detection efficiency of the overall sample for which we do not calculate occurrence rates. For each injection, we randomly drew T_0 from a uniform distribution between 0 and P , ensuring that all possible phases were sampled. This approach allowed us to explore the systemic noise and observing window properties of the ensemble of light curves. We injected these transit signals into each light curve in our sample and scaled the injection with the flux contribution of each star as calculated by `triceratops`. We then passed these injections through `pterodactyls` and calculated the fraction that were recovered as planets to produce a detection efficiency map per cluster as well as an average map for the entire sample. The average detection efficiency map for our entire sample of 5457 stars, and for the 1374 FGK stars in our sample is presented in the top and middle panels, respectively of Figure 4. We find that the overall detection efficiency does not exceed 50% for any bin below $0.1 \frac{R_p}{R_{\star}}$ (akin to a Jupiter-sized planet orbiting a Sun-like star) or $10 R_{\oplus}$, likely due to the effects of flux contamination (Fernandes et al. 2022). In order to gauge how occurrence rates might change with age, we also calculate average detection efficiency maps for two age bins (10–100 Myr and 100–1000 Myr) using injection-recovery results for the stars of corresponding ages. These maps should also account for potential differences in observational biases between the age bins and clusters therein, such as variations in magnitude between young- and intermediate-age stars (Figure 2).

To move from detection efficiency to survey completeness, we also need to calculate the likelihood that a given planet will transit, given by the geometric transit probability:

$$f_{\text{geo}} = \frac{R_{\star}}{a} \quad (1)$$

Here, R_{\star} is the stellar radius, and a is the planet semi-major axis which, through Kepler’s third law, also incorporates a dependence on stellar mass. Because f_{geo} depends on stellar properties, we calculate it per star in order to capture the variation in stellar properties over the range of our sample (e.g., Figure 2), and then multiply each with the sample’s average detection efficiency map. This gives us a set of per-star completeness maps, which we then combine in three ways: one average map for the full sample (presented in Figure 4) and two age-specific average maps for the 10-100 Myr and 100-1000 Myr age bins.

Planet Recovered	TIC ID	Cluster (Age in Myr)	Radius* (R_{\oplus})	Period* (days)	FPP (Gyr-old)	FPP (flat)
HIP 67522 b ^a	166527623	UCL (16±2)	9.72 ^{+0.48} _{-0.47}	6.964±0.026	0.88±0.02	0.75±0.02
AU Mic b ^b	441420236	BetaPic (24±3)	4.02±0.21	8.45±0.04	0.0043±0.0008	0.021±0.002
DS Tuc A b ^c	410214986	THA (45±4)	5.70±0.17	8.138±0.023	0.25±0.03	0.27±0.02
TIC 460950389 b ^d	460950389	IC 2602 (46 ⁺⁶ ₋₅)	3.8±0.2	2.862±0.009	0.0232±0.0006	0.075±0.002
TOI 837 b ^d	460205581	IC 2602 (46 ⁺⁶ ₋₅)	6.9 ^{+0.6} _{-0.4} ; 8.90 ^{+0.74} _{-0.71}	8.325±0.016	0.11±0.06	0.03±0.01
TOI 5358 b ^e	46631742	Pleiades (112±5)	3.52±0.37	2.659±0.003	0.018±0.001	0.081±0.004
TOI 451 b ^f	257605131	PscEri (~120)	1.94 ^{+0.15} _{-0.34}	1.857±0.008	0.057±0.001	0.139±0.004
TOI 451 c ^f	257605131	PscEri (~120)	3.07±0.14	9.19±0.06	0.0330±0.0009	0.127±0.005
TOI 451 d ^f	257605131	PscEri (~120)	4.03±0.15	16.36±0.11	0.005±0.001	0.032±0.005
TOI 4399 b ^g	464646604	ABDMG (149 ⁺⁵¹ ₋₁₉)	3.00 ^{+0.32} _{-0.28}	7.70±0.04	0.056±0.004	0.16±0.01
TOI 1726 b ^h	130181866	UMa (414±23)	2.15±0.10	7.11±0.01	0.011±0.002	0.011±0.006
TOI 1726 c ⁱ	130181866	UMa (414±23)	2.67±0.12	20.54±0.04	0.006±0.003	0.015±0.013
TOI 1726 d ⁱ	130181866	UMa (414±23)	1.084±0.043	4.209±0.005	0.044±0.002	0.049±0.010
K2-25 b ^j	434226736	Hyades (750±100)	3.43 ^{+0.95} _{-0.31}	3.484552±0.000044	0.012±0.003	0.022±0.005
TOI 4364 b ^k	4070275	Hyades (750±100)	2.10 ^{+0.10} _{-0.08}	5.424019±0.000011	0.061±0.005	0.056±0.003
K2-100 b ^l	307733361	Praesepe (790±60)	3.5 ^{+0.2} _{-0.2}	1.673±0.002	0.015±0.002	0.084±0.008
Planet Not Recovered	TIC ID	Cluster (Age in Myr)	Radius ⁺ (R_{\oplus})	Period ⁺ (days)	FPP (Gyr-old)	FPP (flat)
TOI 1227 b ^m	360156606	LCC (15±3)	9.5±0.5	27.36397±0.00011	X	X
HIP 67522 c ⁿ	166527623	UCL (16±2)	8.01 ^{+0.75} _{-0.71}	54 ⁺⁷⁰ _{-0.24}	X	X
AU Mic c ^o	441420236	BetaPic (24±3)	3.51±0.16	~18.86	X	X
K2-136 b ^p	18310799	Hyades (750±100)	0.99 ^{+0.06} _{-0.04}	7.975292 ^{+0.000833} _{-0.000770}	X	X
K2-136 c ^p	18310799	Hyades (750±100)	2.91 ^{+0.11} _{-0.10}	17.307137 ^{+0.000252} _{-0.000284}	X	X
K2-136 d ^p	18310799	Hyades (750±100)	1.45 ^{+0.11} _{-0.08}	25.575065 ^{+0.002418} _{-0.002357}	X	X
HD 283869 b ^q	59873985	Hyades (750±100)	1.96±0.13	106 ⁺⁷⁴ ₋₂₅	X	X
K2-102 b ^l	175262071	Praesepe (790±60)	1.3 ^{+0.1} _{-0.1}	9.915615 ^{+0.001209} _{-0.001195}	X	X
K2-103 b ^l	337632006	Praesepe (790±60)	2.2 ^{+0.2} _{-0.1}	21.169619 ^{+0.001665} _{-0.001729}	X	X
K2-104 b ^l	175194958	Praesepe (790±60)	1.9 ^{+0.2} _{-0.1}	1.974190 ^{+0.000110} _{-0.000110}	X	X
K2 264 b ^r	184914317	Praesepe (790±60)	2.27 ^{+0.20} _{-0.16}	5.839770 ^{+0.000063} _{-0.000061}	X	X
K2 264 c ^r	184914317	Praesepe (790±60)	2.77 ^{+0.20} _{-0.18}	19.663650 ^{+0.000303} _{-0.000306}	X	X
Planet Not Observed	TIC ID	Cluster (Age in Myr)	Radius ⁺ (R_{\oplus})	Period ⁺ (days)	FPP (Gyr-old)	FPP (flat)
K2-33 b ^s	49040478	UppSco (10±3)	5.04 ⁺³⁴ ₋₃₇	5.424865 ^{+0.000035} _{-0.000031}	X	X
K2-95 b ^l	195193025	Praesepe (790±60)	3.7 ^{+0.2} _{-0.2}	10.135091 ^{+0.000495} _{-0.000488}	X	X
EPIC 211901114 b ^l	175291050	Praesepe (790±60)	9.6 ^{+5.3} _{-4.8}	1.648932 ^{+0.000071} _{-0.000069}	X	X
K2-101 b ^l	175265494	Praesepe (790±60)	2.0 ^{+0.1} _{-0.1}	14.677286 ^{+0.000828} _{-0.000804}	X	X

Table 1. List of confirmed planets and planet candidates in our sample of young stellar clusters and moving groups. Age and cluster memberships are from [Gagné et al. \(2018\)](#) and [Babusiaux et al. \(2018\)](#). *Recovered radii and orbital periods consistent with published literature values; ⁺Published radii and orbital periods due to non-recovery. False Positive Probability (FPP) is derived using `triceratops` assuming both Gyr-old and flat priors. References: (a) [Rizzuto et al. \(2020\)](#); (b) [Plavchan et al. \(2020\)](#); (c) [Newton et al. \(2019\)](#); (d) [Nardiello et al. \(2020\)](#); (e) ExoFOP; (f) [Newton et al. \(2021\)](#); (g) [Zhou et al. \(2022\)](#); (h) [Capistrant et al. \(2024\)](#); (i) [Mann et al. \(2020\)](#); (j) [Mann et al. \(2016a\)](#); (k) [Distler et al. \(2024\)](#); (l) [Mann et al. \(2017\)](#); (m) [Mann et al. \(2022\)](#); (n) [Barber et al. \(2024\)](#); (o) [Cale et al. \(2021\)](#); (p) [Mann et al. \(2018\)](#); (q) [Vanderburg et al. \(2018\)](#); (r) [Rizzuto et al. \(2018\)](#); (s) [Mann et al. \(2016b\)](#).

Using these completeness measurements, we can then provide estimates for the intrinsic planet occurrence rate (η). There are multiple ways to measure planet occurrence rates, and each technique carries both advantages and disadvantages. The inverse detection efficiency method provides direct measurements of planet occurrence rates in regimes with planet detections, but strug-

gles to outline the distribution of occurrence rates with planet properties when samples are sparse. Meanwhile, occurrence rate forward modeling allows us to parametrically describe how occurrence rates are distributed, but requires imposing a specific functional form. We opt to use both techniques in the following subsections, so that we might better characterize – both natively and para-

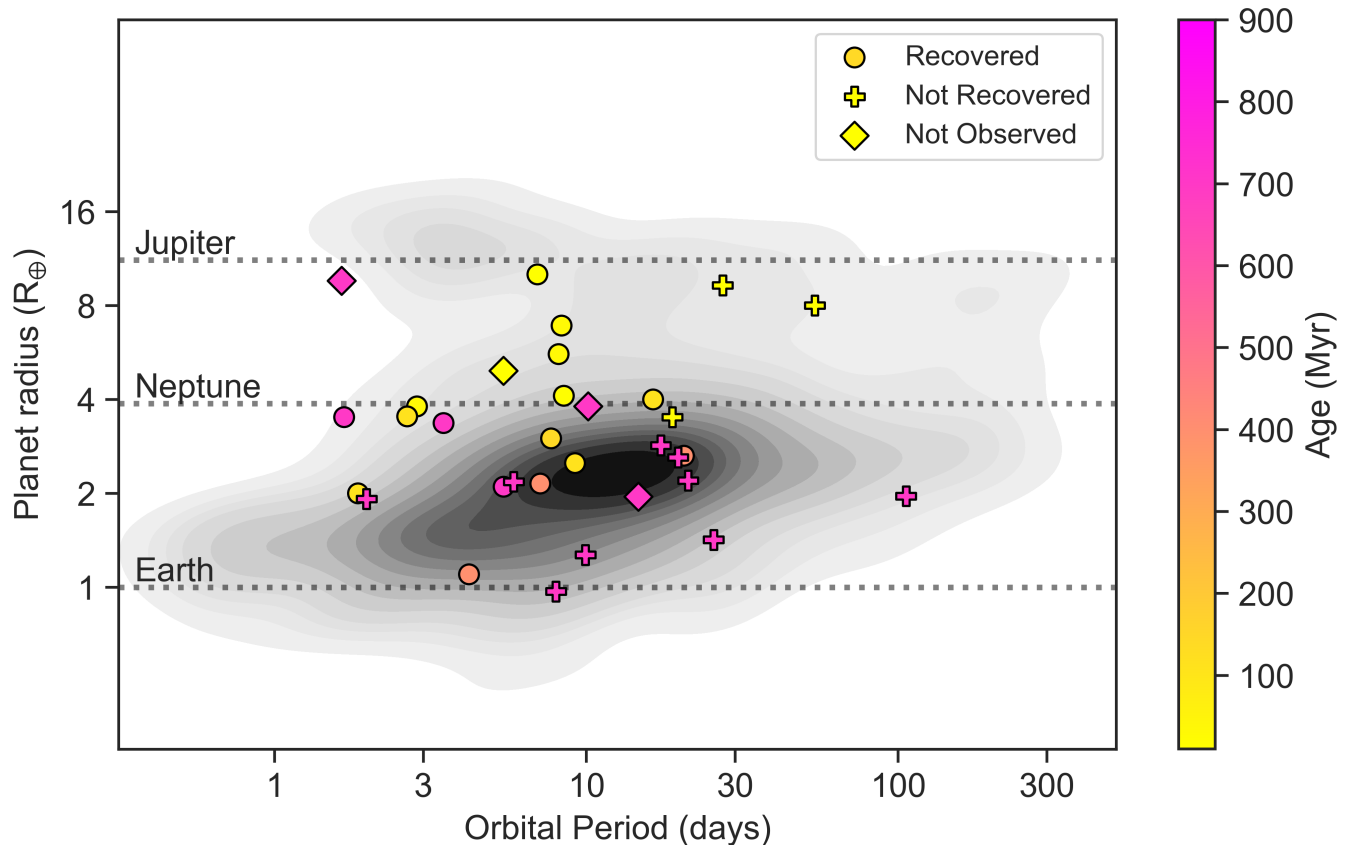


Figure 3. Comparison of the young transiting planet population in our sample (color-coded by age), and the Gyr-old transiting planet population (gray contours). Young gas-rich planets appear to be puffier, and “shrink” as they age, thereby populating gaps in the Gyr-old distribution, as indicated by our statistical analysis of this sample.

metrically – the occurrence rates of our young planet sample.

4.2. Inverse Detection Efficiency Method

We first employed the inverse detection efficiency method, where occurrence rates η are calculated in bins of orbital period and planet radius using:

$$\eta_{\text{bin}} = \frac{1}{n_*} \sum_j^{n_p} \frac{1}{\text{comp}_j}, \quad (2)$$

where comp_j represents the survey completeness evaluated at the properties of the j^{th} planet, n_p denotes the number of detected planets in the bin, and n_* stands for the number of surveyed stars. The uncertainty on the occurrence rate was computed from the square root of the number of detected planets in the bin, assuming Poissonian statistics.

In our analysis, we focused on planets with radii between $1.8\text{--}10 R_{\oplus}$ within 12 days (roughly half a TESS sector) to examine the primordial population of sub-Neptunes and Neptunes. With an average detection

efficiency of 40%, we derived an occurrence rate of $54.0 \pm 16.3\%$ for our young cluster sample.

For the same orbital period and planet radius bins, we also calculated an occurrence rate from the *Kepler* sample of Gyr-old FGK (Sun-like) stars. As in Bergsten et al. (2022), we employed the final *Kepler* data release (Thompson et al. 2018) supplemented with the Berger et al. (2020b) catalog of *Gaia*-revised stellar properties (Gaia Collaboration et al. 2018). We isolated a sample of 114,515 dwarf stars with masses between $0.56\text{--}1.63 M_{\odot}$, based on FGK stellar mass range from Pecaut & Mamajek (2013) and the Huber et al. (2016) criterion where a star is considered a dwarf if :

$$\log g > \frac{1}{4.671} \arctan \left(\frac{T_{\text{eff}} - 6300}{-67.172} \right) + 3.876. \quad (3)$$

Among these stars are 554 confirmed and candidate planets (as reported in Thompson et al. 2018) with orbital periods between 1–12 days and *Gaia*-updated planet radii between $1.8\text{--}10 R_{\oplus}$.

Using this population of stars and planets, alongside a set of per-star completeness maps from Bergsten et al. (2022), we computed an occurrence rate value of

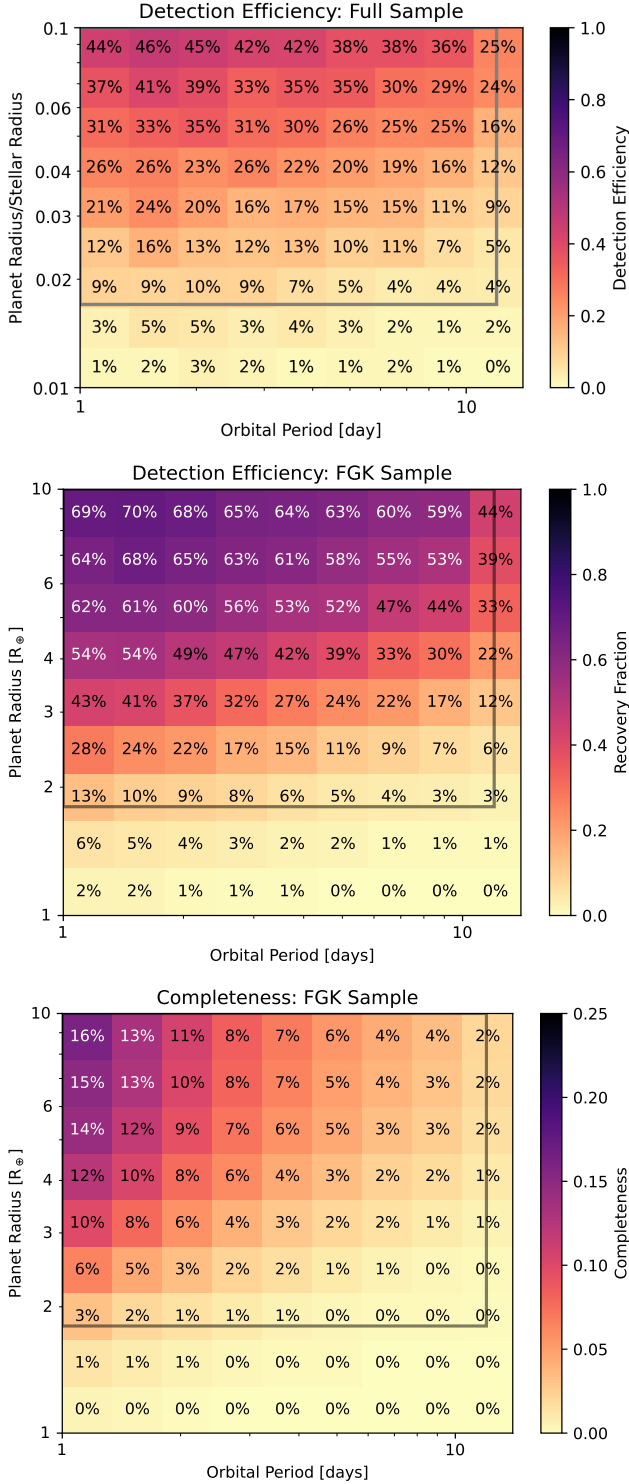


Figure 4. **Top:** Overall detection efficiency of pterodactyls in $\frac{R_p}{R_*}$ space for the full sample. **Center:** Detection efficiency of the FGK stars in our sample. **Bottom:** Completeness of the FGK sample which combines the detection efficiency with the geometric transit probability. The black box denotes the bin over which the intrinsic occurrence rates were calculated i.e., sub-Neptunes and Neptunes ($1.8\text{--}10 R_\oplus$) within 12 days.

$7.79 \pm 0.33\%$, appreciably lower than our derived value for young clusters. If the measured decrease in planet occurrence is due to larger planets shrinking to smaller radii below our $1.8 R_\oplus$ cut-off, then it is possible that a *Kepler* occurrence rate which includes these smaller planets may be more similar to our young planet sample. To investigate this, we reevaluated occurrence rates from the *Kepler* sample while including planets down to $0.3 R_\oplus$. From the inverse detection efficiency method, we find an occurrence of $39.5 \pm 1.0\%$ while including *Kepler* planets down to $0.3 R_\oplus$. Thus, the derived young star planet occurrence rate ($54.0 \pm 16.3\%$) is within 1σ with that of *Kepler* assuming most planets lose their atmospheres over time.

To explore how the occurrence of our sample might further depend on planet properties, we split our sample into two bins of equal log-width in orbital period and applied the inverse detection efficiency method; separately, we also repeated this using three bins of planet radius. The resulting values are plotted in Figure 5, where we note a tendency for occurrence rates to increase with orbital period and decrease with planet radius. These trends have also been demonstrated in the *Kepler* Gyr-old population (see e.g., Petigura et al. 2018; Bergsten et al. 2022), as indicated in the *Kepler* values also plotted in Figure 5.

Furthermore, we split our sample into two age bins with equal numbers of planets: 10–100 Myr and 100–1000 Myr. While the uncertainties on these points are necessarily larger than those of the full young sample, we note a 1σ distinct offset between values from the inverse detection efficiency method. To better understand and quantify the differences in these trends between our young sample and *Kepler*, we employ occurrence rate forward modeling to profile these trends over a more continuous distribution of periods and radii.

4.3. Occurrence Rate Modeling

Separately from the previous subsection, we also fit parametric models to our young planet sample to better understand the distribution of planet occurrence rates. We adopt the approach of Youdin (2011) and Burke et al. (2015) to model the two-dimensional occurrence distribution, following the methodology of Bergsten et al. (2022).

Our model includes three free parameters: F_0 represents the average number of planets per star, while the parameters α and β define the slope of a power law in orbital period and planet radius, respectively. Similar models will often use a broken power law in orbital period, although this break typically occurs somewhere around $\sim 10\text{--}12$ days for FGK stars (see e.g., Mulders

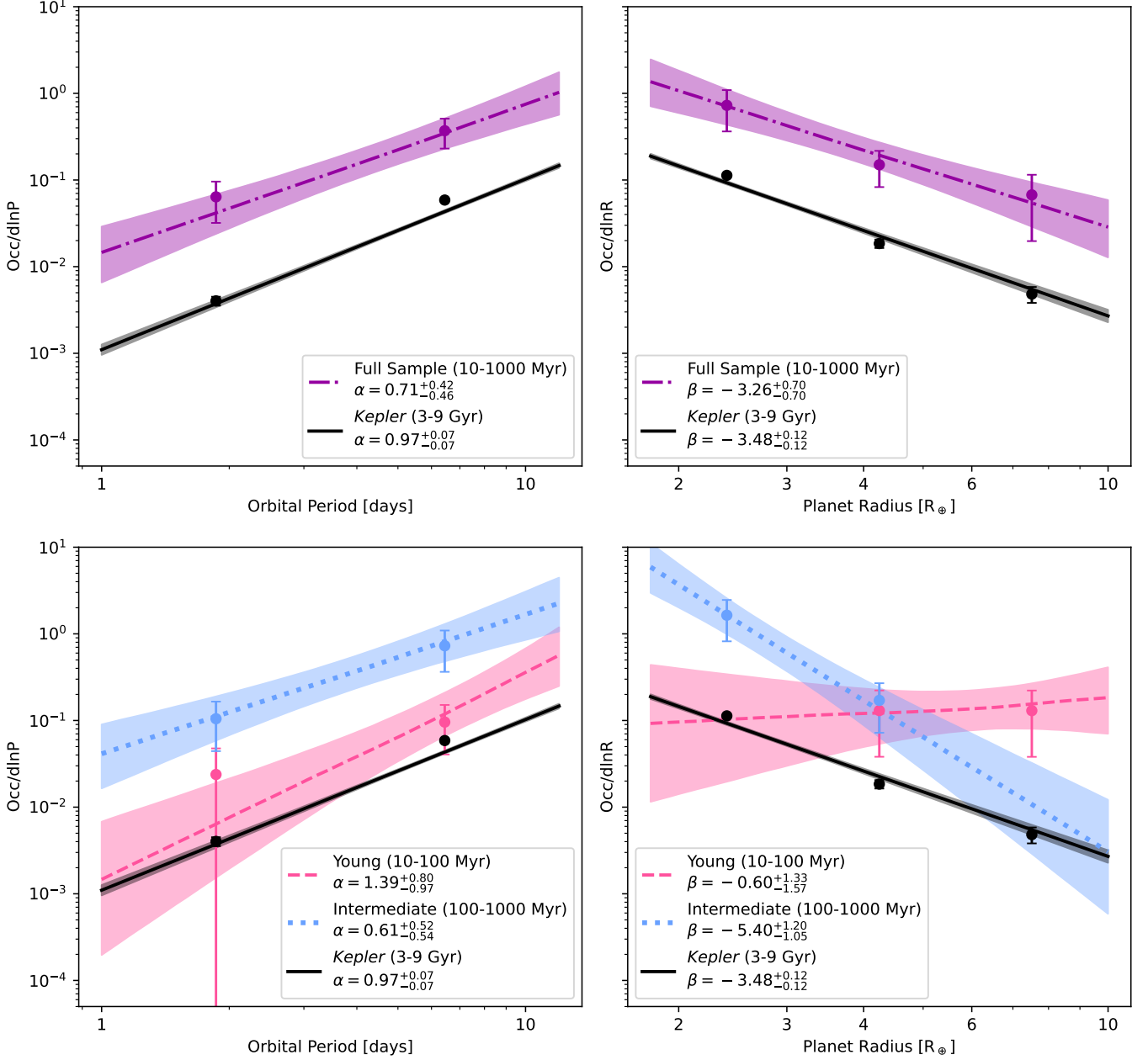


Figure 5. Comparison of the *Kepler*'s inverse detection efficiency values (circles), our best fit occurrence models (lines) in orbital period and radius space, respectively, with **Top:** our entire sample (10–1000 Myr), and **Bottom:** split into our young (10–100 Myr) and intermediate (100–1000 Myr).

et al. 2018; Bergsten et al. 2022). As our sample is limited to planets within 12 days, a single power law is sufficient for our study. Our model thus takes the form:

$$\frac{d^2 f}{dP dR} = F_0 C_n P^\alpha R^\beta \quad (4)$$

where C_n is the normalization constant from Burke et al. (2015). This function requires integrating the sum of each star's completeness (as described in Section 4.1) over a grid of orbital periods and planet radii. Model parameters were optimized through a Markov-chain Monte

Carlo process (emcee, Foreman-Mackey et al. 2013) to minimize the corresponding likelihood function (Eqn. 9 in Burke et al. 2015). We used 64 walkers and ran for 20,000 steps (at least 50 times the autocorrelation time τ), with the first 1,000 (at least 2τ) discarded for burn-in.

To gauge if any model parameters changed with age, we fit separate models to three age bins: 10–100 Myr, 100–1000 Myr, and the full young sample. Additionally, to enable better comparison with the *Kepler* FGK sam-

ple, we include a model fit as described above, but using *Kepler* data and summed per-star completeness maps as in Bergsten et al. (2022).

5. RESULTS AND DISCUSSION

In Figure 5, we plot occurrence rates and uncertainties from the inverse detection efficiency method alongside our best-fit occurrence models. The model free parameters are plotted in Figure 6 and listed in Table 2, with the median and lower/upper 1σ uncertainty values taken from the 50th and 16th/84th percentiles, respectively.

Our models find that the occurrence rate of young planets is higher than the Gyr-old *Kepler* population, also seen with the inverse detection efficiency method as described in Section 4.2. From Table 2, the average number of planets per star for our full young sample is $F_0 = 63.62^{+31.58}_{-22.16}\%$, which is distinct from the *Kepler* value of $7.98^{+0.37}_{-0.35}\%$ at the 2.5σ level. Additionally, we measure $F_0 = 25.89^{+20.18}_{-11.67}\%$ for our younger 10–100 Myr age bin consistent with Vach et al. (2024), and $F_0 = 148.93^{+93.60}_{-61.10}\%$ for our intermediate 100–1000 Myr age bin consistent with Christiansen et al. (2023). We note that the intermediate bin’s value is larger and more uncertain than that of the younger, such that that our two age bins are distinct at the 1.9σ level (see e.g., Figure 6). We present this difference between the age bins with caution, as it could be an artifact of small number statistics, or imposing a functional form that artificially inflates occurrence in the older bin (e.g., fitting a power law in radius space out to $10 R_{\oplus}$ despite no planets exceeding $4 R_{\oplus}$ in that bin).

Regarding the shape of the best-fit occurrence distributions, we measure a significant change in the slope of the occurrence-radius distribution with age, but not in the occurrence-period distribution. All of our best-fit occurrence-period slopes, for both the young stars and the *Kepler* sample(s), are consistent at 1σ . Meanwhile, we find tentative (2.2σ) evidence that the occurrence-radius distribution may steepen with age, from $\beta = -0.60^{+1.57}_{-1.33}$ in our youngest age bin to $-3.48^{+0.12}_{-0.12}$ with *Kepler*. The latter is similar to the $\beta = -3.26^{+0.70}_{-0.70}$ value measured for our full young sample, and we neglect discussing the intermediate age bin which only has coverage of smaller ($< 4 R_{\oplus}$) planets.

5.1. Interpretations and Implications

Here we discuss potential explanations for the results described above and their implications for planet formation/evolution. We precede this discussion with a note that our coverage of stellar age begins at 10 Myr, offering only a partial view of planet formation and evolution.

Evidence from older populations shows that the occurrence of sub-Neptunes ($< 4 R_{\oplus}$) increases with or-

bit period up to ~ 10 days, beyond which it flattens in log-period space, forming a plateau across all stellar types (F, G, K, and M) in Gyr-old dwarfs (Mulders et al. 2015). This turnover likely reflects the gas disk’s truncation by the host star’s magnetosphere at the corotation radius (see also Lee & Chiang 2017), suggesting that planets often migrate to the gas disk truncation radius early on. These findings suggest that early disk-driven migration, either of fully formed planets or their building blocks, plays a key role in shaping the inner architecture of planetary systems and that planets with periods < 10 days have been most influenced by stellar tides over time. Our survey is sensitive to young (< 1 Gyr) sub-Neptunes primarily inside 10 days, and the finding of increased occurrence between the 10–100 Myr and 100–1000 Myr age bins aligns with the long timescales required for tides to bring planets within the disk truncation radius (e.g., Jackson et al. 2009). The presence of planets with periods < 10 days in our youngest age bin suggests that migration to – or formation at – such short periods must occur within the first 10–100 Myr. Given the lack of substantial material within the truncation radius, in-situ formation of planets at such short periods is unlikely but cannot be entirely ruled out.

Next, the observed increase in occurrence between our younger and intermediate age bins, from $F_0 = 25.89^{+20.18}_{-11.67}\%$ to $148.93^{+93.60}_{-61.10}\%$, could be indicative of further migration. If the majority of large, short-period planets form or arrive at their final location during the gas disk stage, we would expect a decline in occurrence rates with age driven by atmospheric cooling and escape. The observed rise in occurrence rates here would thus suggest a later arrival of planets between 100 Myr and 1 Gyr, possibly through tidal migration. If a planet is disturbed onto an elliptical orbit through processes like planet-planet scattering (e.g., Rasio & Ford 1996; Weidenschilling & Marzari 1996), secular cycles (e.g., Wu & Murray 2003), or secular chaos (e.g., Petrovich et al. 2019), it can migrate via tides (e.g., Hut 1981; Eggleton et al. 1998) raised on the planet (e.g., Socrates et al. 2012). Regardless of orbital eccentricity, a planet can also migrate via tides raised on the star. Stellar tides could further reduce a planet’s period beyond the truncation radius to explain the population of planets inside 10 days (Lee & Chiang 2017) which our survey is mostly sensitive to. The processes disturbing planets into elliptical orbits can operate over a range of timescales. Moreover, the planet’s initial position and eccentricity—as well as uncertain quantities like the tidal quality factor—set the tidal migration timescale, which can span many orders of magnitude. Thus, we expect new contri-

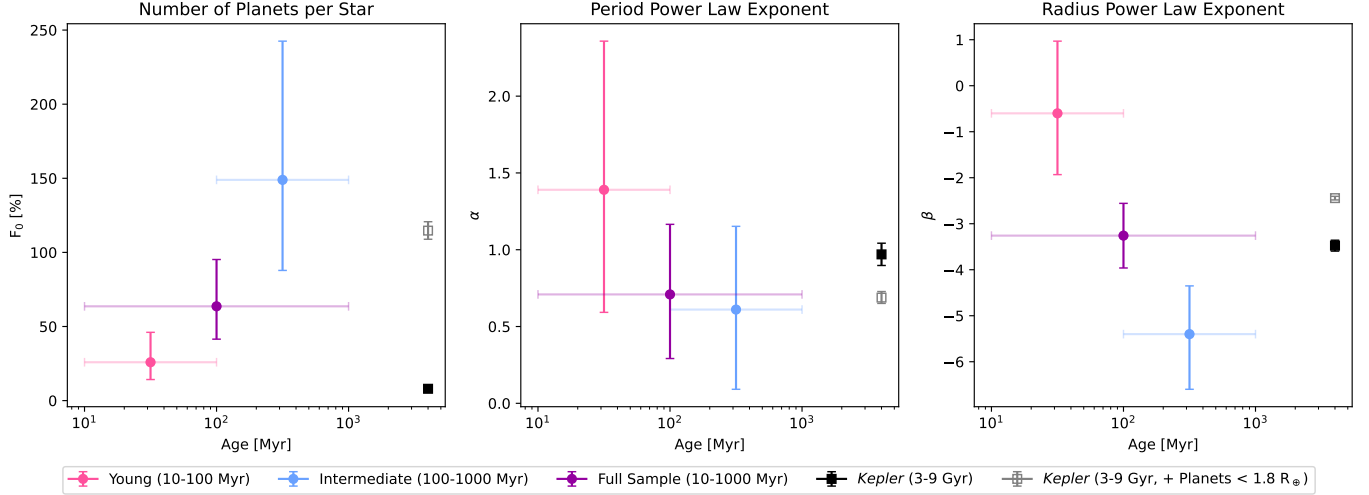


Figure 6. Comparison of the number of planets per star (F_0), Period (α), and Radius (β) exponents across the different age bins.

Sample (FGK)	F_0 [%]	α	β
10–100 Myr	$25.89^{+20.18}_{-11.67}$	$1.39^{+0.97}_{-0.80}$	$-0.60^{+1.57}_{-1.33}$
100–1000 Myr	$148.93^{+93.60}_{-61.10}$	$0.61^{+0.54}_{-0.52}$	$-5.40^{+1.05}_{-1.20}$
10–1000 Myr	$63.62^{+31.58}_{-22.16}$	$0.71^{+0.46}_{-0.42}$	$-3.26^{+0.70}_{-0.70}$
<i>Kepler</i> (Gyr-old)	$7.98^{+0.37}_{-0.35}$	$0.97^{+0.07}_{-0.07}$	$-3.48^{+0.12}_{-0.12}$
<i>Kepler</i> (Gyr-old, + Planets $< 1.8 R_{\oplus}$)	$114.70^{+6.00}_{-5.83}$	$0.69^{+0.04}_{-0.04}$	$-2.44^{+0.04}_{-0.04}$

Table 2. Best-fit and 1σ model parameters for the two age bins of our sample, the full young sample, and the *Kepler* Gyr-old sample.

butions from tidal migration in every order of magnitude of age (e.g., as argued by Safsten et al. 2020).

One caveat is that migration would also likely cause the occurrence-period slope to become more shallow with time, as planets become less sharply-peaked near the truncation radius and more evenly distributed across shorter periods. Unfortunately, we cannot provide complement the observed trend in F_0 with evidence for the evolving occurrence-period slope due to large uncertainties driven by small sample sizes. While a steeper slope at young ages is plausible (Figure 6) within our uncertainties, a slope that does not change with age is also possible, so constraining the true behavior of this parameter ultimately requires a larger dataset. If the slope remains unchanged with age, it may suggest that planets within 1–12 days either do not migrate or experience a migratory process that acts uniformly in log-period space.

Moving from our young sample to the Gyr-old *Kepler* population, the moderately significant decrease in occurrence between the intermediate age bin and the *Kepler* sample (from $F_0 = 148.93^{+93.60}_{-61.10}$ to $7.98^{+0.37}_{-0.35}$) could be indicative of planetary atmospheric mass loss. Atmospheric thermal evolution and mass loss play important

roles in controlling the size distribution of planets hosting H/He-dominated atmospheres. Many studies have shown that planetary atmospheres can significantly contract with time, as a direct result of thermal cooling and stellar-driven escape (e.g. Owen & Wu 2013; Lopez & Fortney 2013). Of note, core-powered mass loss relies on a bolometrically heated outflow (Gupta & Schlichting 2019), whereas photoevaporative mass loss relies on XUV-driven outflow (Rogers & Owen 2021).

While the complex physical interplay between core-powered and photoevaporative mass loss is an area of active research (e.g. Owen & Schlichting 2024; Rogers et al. 2024), one would expect the planet demographics to change with time as a result of these processes. Specifically, there should be a higher abundance of large planets that will eventually contract to become sub-Neptunes, or super-Earths if their atmospheres are completely stripped. Our results agree with this general trend, demonstrated in Figure 5 and the evolution of free parameters for the occurrence F_0 and occurrence-radius slope β (Figure 6, Table 2). Comparing the same 1.8–10 R_{\oplus} range for our intermediate age bin and *Kepler*, we see a higher planet occurrence around young stars with a flatter occurrence-radius distribution (both

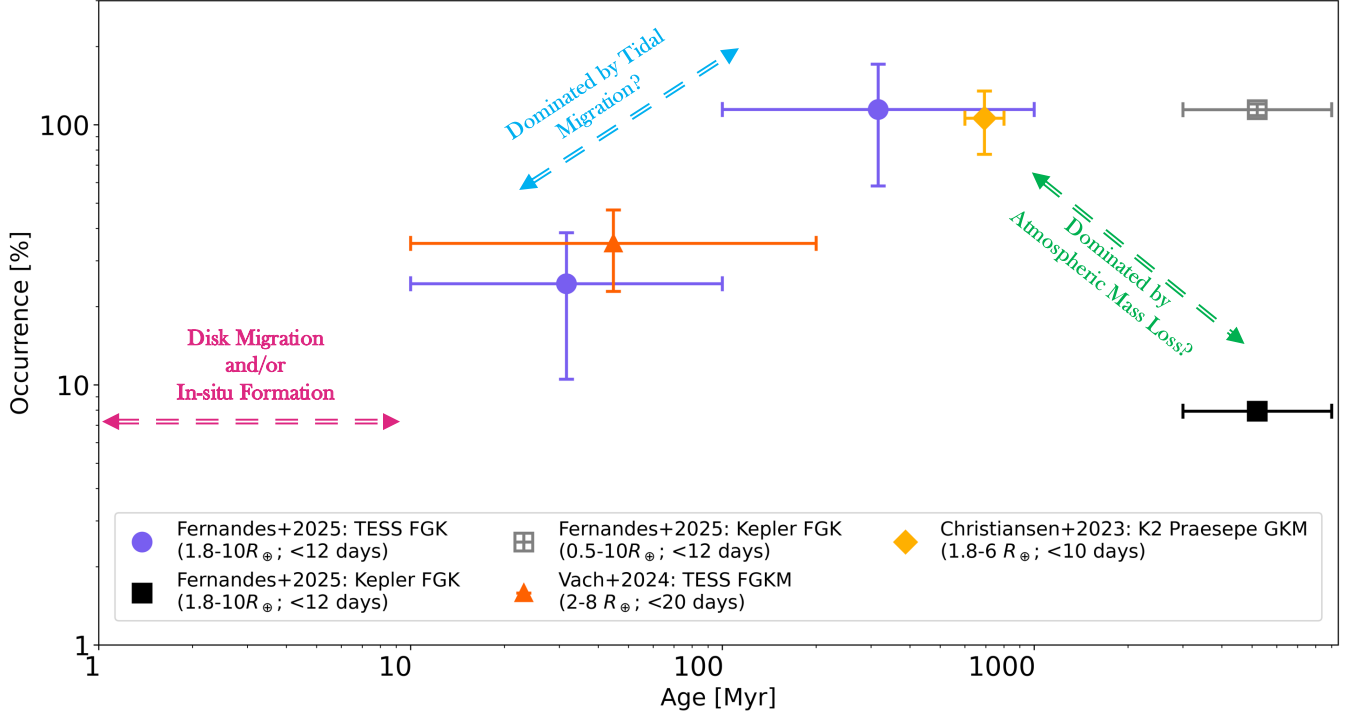


Figure 7. Comparison of occurrence rates for sub-Neptunes and Neptunes from different surveys, with the various underlying mechanisms and their timelines depicted with dashed arrows.

true at 2.5σ), indicating an increased fraction of puffer planets. When planets smaller than $1.8 R_{\oplus}$ (i.e., the super-Earths) are accounted for, the occurrence of Gyr-old planets becomes comparable to that of intermediate-age planets ($F_0 = 114.70^{+6.00}_{-5.83}$ and $148.93^{+93.60}_{-61.10}$, respectively), consistent with the idea of planets shrinking below our $1.8 R_{\oplus}$ cutoff with age due to atmospheric mass loss processes.

Given that radius contraction due to thermal cooling is not expected to significantly shrink planets and most of it occurs before 1 Gyr (e.g., Mordasini et al. 2012), this suggests that gas-rich planets are losing their atmospheres to become Super-Earths on Gyr-timescales, consistent with previous observational studies (Berger et al. 2020a; David et al. 2021). This poses an apparent challenge to photoevaporation models because the bulk of the atmospheric loss due to photoevaporation is often predicted to take place during the first 100 Myr (Rogers & Owen 2021) when a significant fraction of the planets may still be migrating to their final location. This view of the problem, however, may be overly simplistic because both photoevaporation and core-powered mass loss continue at varying levels on Gyr-timescales. Coupled models of planet formation and envelope loss due to different mechanisms will help to shed light on planet evolution based on our results. We note that,

since our completeness is too low for young, small planets below $1.8 R_{\oplus}$, we are unable to probe any increase in occurrence of super-Earths, as would be predicted by mass loss models. However, we note that this process is critical to take into account to properly estimate the occurrence of Earth-size planets in the habitable zone (Pascucci et al. 2019; Bergsten et al. 2022).

Tidal disruption may also play a role, destroying either the entire planet or its atmosphere (e.g., Faber et al. 2005; Guillochon et al. 2011). Planets with orbital periods shorter than the stellar spin period transfer angular momentum to spin up their stars, so tidal disruption is the ultimate fate of migration driven by tides raised on the star. Tidal disruption is also the ultimate fate of tidal migration driven by tides raised on the planet if the planet’s periape comes within the Roche limit. As an end state of tidal migration, tidal disruption occurs over many orders of magnitude in timescales. It is not obvious that the balance between arriving and disrupted planets would raise the occurrence rate from 100 Myr to 1 Gyr but substantially drop it at 1–10 Gyr. Therefore, it seems unlikely that tidal disruption is the predominant cause of the drop.

Another explanation for a change in the occurrence rate of planets with time is not that the planets themselves are evolving, but that planetary systems them-

selves form differently at different Galactic epochs. Christiansen et al. (2023) and references therein discuss a variety of Galactic environmental factors that could impact planet formation that have changed with time. Stars born at earlier times can be significantly more strongly externally irradiated by higher Galactic star formation rates, which could reduce both protoplanetary disk lifetimes and the materials remaining for planet formation. Stars born at earlier times are also typically born in more highly dynamically clustered environments, which could lead to frequent interactions between nearby stars that could destabilize the planetary systems that did form. Unlike the mass-loss mechanisms described above, there are currently few published predictions of the extent to which these processes may impact planet formation to test, however at this stage these effects cannot be ruled out as the cause of some of the trends seen here.

5.2. Hot Neptune Desert

We also calculated occurrence rates in the hot Neptune desert, here defined as planets with radii between $3\text{--}10 R_{\oplus}$ and orbital periods between 1–4 days (Beaugé & Nesvorný 2013). The hot Neptune desert hosts some of the most highly irradiated exoplanets. As such, we expect atmospheric escape to be a dominant driver in the radius evolution of planets within the desert. Using the inverse detection efficiency method, we find an occurrence rate of $6.28 \pm 3.14\%$ for young planets in our sample. Further dividing our sample, we find $2.96 \pm 2.96\%$ for the occurrence rate of planets between 10–100 Myr (note that $n = 1$ here), and the occurrence rate of $9.76 \pm 5.64\%$ for between 100–1000 Myr. The occurrence rate of young planets is therefore higher than the occurrence rate of $0.19 \pm 0.04\%$ from *Kepler* (1.9σ), which supports the notion that atmospheric escape is dominant for such planets, causing them to contract below $\sim 1.8 R_{\oplus}$ over time. This result, however, is only weakly significant. Larger sample sizes would reduce the uncertainties, providing a more clear picture of how this region of planet parameter space evolves with age. In addition, we note that our survey is not sensitive to planets below $1.8 R_{\oplus}$, so a more sensitive characterization of smaller planets in young clusters may provide more insights.

6. SUMMARY

In this study, we expanded on our work in Fernandes et al. (2022) and Fernandes & Hardegree-Ullman et al. (2023), and calculate the occurrence rates of short-period sub-Neptunes and Neptunes in nearby (<200 pc) young clusters and moving groups (10 Myr–1 Gyr) using

TESS EM1 FFIs. These planets provide insight into a population much closer in time to the primordial planet population. By comparing the intrinsic occurrence rates of the young planets with that of the mature *Kepler* population, we can begin to piece together how planetary systems have evolved with time. In our analysis, we find that:

- For our entire sample (10 Myr–1 Gyr), the intrinsic occurrence rate for young, short-period sub-Neptunes and Neptunes ($63.62^{+31.58}_{-22.16}\%$) is higher than that of older planets observed by *Kepler* ($7.98^{+0.37}_{-0.35}\%$), for the same period and radius bins, confirming previous results (e.g., Christiansen et al. 2023; Vach et al. 2024).
- Binning our sample by age, the occurrence increases from young (10–100 Myr) to intermediate (100–1000 Myr) ages, from $25.89^{+20.18}_{-11.67}\%$ to $148.93^{+93.60}_{-61.10}\%$. This distinction is significant at the 1.9σ level and, if real, suggests a later arrival of planets between 100 Myr and 1 Gyr, possibly through tidal migration in which planets perturbed onto elliptical orbits can migrate via tides raised on the planet or the star. Tidal migration processes can operate over a range of timescales, contributing to occurrence rates in different age bins. If tidal migration increases rates from 100 Myr to 1 Gyr, it must be masked by other declines in the 1–10 Gyr bin.
- The occurrence also decreases from $F_0 = 148.93^{+93.60}_{-61.10}$ at intermediate ages to $7.98^{+0.37}_{-0.35}$ with *Kepler*. We also observe a steepening of the occurrence-radius distribution with age (from $\beta = -0.60^{+1.57}_{-1.33}$ in our youngest age bin to $-3.48^{+0.12}_{-0.12}$ with *Kepler*). These results indicate a population of planets undergoing atmospheric thermal evolution and mass loss, including core-powered and photoevaporative mass loss. These processes play important roles in controlling the size distribution of H/He-dominated planets, and cause planets to contract over time due to thermal cooling and stellar-driven escape.
- The occurrence rate in the hot Neptune desert ($3\text{--}10 R_{\oplus}$, 1–4 days), using inverse detection efficiency, is $6.28 \pm 3.14\%$ for young planets (10 Myr–1 Gyr). This is significantly higher than *Kepler*'s $0.19 \pm 0.04\%$, suggesting that planets that initially formed in the hot Neptune Desert may shrink below $1.8 R_{\oplus}$ due to extreme atmospheric escape.

While we find evidence of post-disk migration and atmospheric mass loss sculpting the population of short-period planets over time, there is still much left to be done. For example, we are unable to determine whether

the occurrence-period distribution changes with age due to large uncertainties driven by our small sample size. Overall, there is a need to detect more young planets. Currently, there are fewer than 40 young planets found in both clusters/moving groups and young field stars, compared to thousands around Gyr-old field stars with *Kepler*. Increasing the sample of young planets will enable a more statistically robust comparison of the intrinsic occurrence rates with time.

There is a need to simultaneously compute the occurrence of longer-period, young planets (>12 days), and compare it with that of short-period young planets to fully understand the role of post-disk migration. To evaluate if atmospheric mass loss is a dominant driver in the radius evolution of gas-rich planets we need to detect planets smaller than $1.8 R_{\oplus}$ (super-Earths) and compare their occurrence with that of gas-rich planets over time. Given that the light curves of young stars are highly variable, making it challenging to detect small planets, we need more precise light curves, which upcoming missions like PLATO (Rauer et al. 2024) can likely provide.

Furthermore, the atmospheres of young planets can help provide context on the conditions under which planets form. By studying the volatile composition of young planetary atmospheres, we can begin to distinguish between in-situ and ex-situ (plus migration) scenarios, placing constraints on the timescales of planet formation. The composition of these planetary atmospheres, paired with the activity levels of the host stars, can help us better understand the efficiency and timescales of atmospheric mass loss mechanisms. Through these investigations, we can significantly enhance our understanding of planetary formation, migration, and evolution processes, providing a clearer picture of the dynamic history of planetary systems.

Software: `pterodactyls` (Fernandes 2022), `NumPy` (van der Walt et al. 2011), `SciPy` (Jones et al. 2001–), `Matplotlib` (Hunter 2007), `eleanor` (Feinstein et al. 2019), `Wotan` (Hippke et al. 2019), `transitleastsquares` (Hippke & Heller 2019), `vetting` (Hedges 2021), `triceratops` (Giacalone et al. 2021), `EDI-Vetter Unplugged` (Zink 2019), `EXOTIC` (Zellem et al. 2020), `epos` (Mulders et al. 2018), `emcee` (Foreman-Mackey et al. 2013), `corner` (Foreman-Mackey 2016)

7. ACKNOWLEDGEMENTS

R.B.F. would like to thank Eric Ford for their expertise, assistance and, invaluable insights throughout this work. I.P., G.B., and K. C. acknowledge support from the NASA Astrophysics Data Analysis Program under grant No. 80NSSC20K0446. G.D.M. acknowledges sup-

port from FONDECYT project 11221206, from ANID — Millennium Science Initiative — ICN12_009, and the ANID BASAL project FB210003. S.G. is supported by an NSF Astronomy and Astrophysics Postdoctoral Fellowship under award AST-2303922. A.G. is grateful to the Heising-Simons Foundation for the 51 Pegasi b Fellowship and to Princeton University for the Harry H. Hess Fellowship and the Future Faculty in Physical Sciences Fellowship. T.T.K acknowledges support by the NASA/XRP grant 80NSSC23K0260.

The Center for Exoplanets and Habitable Worlds and the Penn State Extraterrestrial Intelligence Center are supported by Penn State and its Eberly College of Science. Computations for this research were performed on the Pennsylvania State University’s Institute for Computational and Data Sciences’ Roar supercomputer. Part of this research was carried out in part at the Jet Propulsion Laboratory, California Institute of Technology, under a contract with the National Aeronautics and Space Administration (80NM0018D0004). This paper includes data collected by the TESS mission. Funding for the TESS mission is provided by the NASA’s Science Mission Directorate. This material is based upon work supported by the National Aeronautics and Space Administration under Agreement No. 80NSSC21K0593 for the program “Alien Earths”. The results reported herein benefited from collaborations and/or information exchange within NASA’s Nexus for Exoplanet System Science (NExSS) research coordination network sponsored by NASA’s Science Mission Directorate. This research has made use of the NASA Exoplanet Archive, which is operated by the California Institute of Technology, under contract with the National Aeronautics and Space Administration under the Exoplanet Exploration Program.

REFERENCES

- Babusiaux, C., van Leeuwen, F., Barstow, M., et al. 2018, *Astronomy & astrophysics*, 616, A10
- Barber, M. G., Thao, P. C., Mann, A. W., et al. 2024, *ApJL*, 973, L30
- Beaugé, C., & Nesvorný, D. 2013, *ApJ*, 763, 12
- Berger, T. A., Huber, D., Gaidos, E., van Saders, J. L., & Weiss, L. M. 2020a, *AJ*, 160, 108
- Berger, T. A., Huber, D., van Saders, J. L., et al. 2020b, *arXiv e-prints*, arXiv:2001.07737
- Bergsten, G. J., Pascucci, I., Mulders, G. D., Fernandes, R. B., & Koskinen, T. T. 2022, *AJ*, 164, 190
- Borucki, W. J., Koch, D., Basri, G., et al. 2010, *Science*, 327, 977
- Bouma, L., Hartman, J., Brahm, R., et al. 2020, *The Astronomical Journal*, 160, 239
- Bourrier, V., Attia, O., Mallonn, M., et al. 2023, *A&A*, 669, A63
- Burke, C. J., Christiansen, J. L., Mullally, F., et al. 2015, *ApJ*, 809, 8
- Caldwell, D. A., Tenenbaum, P., Twicken, J. D., et al. 2020, *Research Notes of the American Astronomical Society*, 4, 201
- Cale, B. L., Reefer, M., Plavchan, P., et al. 2021, *AJ*, 162, 295
- Capistrant, B. K., Soares-Furtado, M., Vanderburg, A., et al. 2024, *AJ*, 167, 54
- Christiansen, J. L., Zink, J. K., Hardegree-Ullman, K. K., et al. 2023, *AJ*, 166, 248
- Ciardi, D. R., Beichman, C. A., Horch, E. P., & Howell, S. B. 2015, *The Astrophysical Journal*, 805, 16
- Ciardi, D. R., Crossfield, I. J. M., Feinstein, A. D., et al. 2018, *AJ*, 155, 10
- Cody, A. M., Stauffer, J., Baglin, A., et al. 2014, *AJ*, 147, 82
- Curtis, J. L., Agüeros, M. A., Mamajek, E. E., Wright, J. T., & Cummings, J. D. 2019, *AJ*, 158, 77
- David, T. J., Contardo, G., Sandoval, A., et al. 2021, *AJ*, 161, 265
- Distler, A., Soares-Furtado, M., Vanderburg, A., et al. 2024, *arXiv e-prints*, arXiv:2410.11990
- Dong, S., & Zhu, Z. 2013, *ApJ*, 778, 53
- Dressing, C. D., & Charbonneau, D. 2015, *The Astrophysical Journal*, 807, 45
- Duchêne, G., & Kraus, A. 2013, *Annual Review of Astronomy and Astrophysics*, 51, 269
- Eggleton, P. P., Kiseleva, L. G., & Hut, P. 1998, *ApJ*, 499, 853
- Ercolano, B., & Pascucci, I. 2017, *Royal Society Open Science*, 4, 170114
- Faber, J. A., Rasio, F. A., & Willems, B. 2005, *Icarus*, 175, 248
- Feinstein, A. D., Montet, B. T., Foreman-Mackey, D., et al. 2019, *Publications of the Astronomical Society of the Pacific*, 131, 094502
- Fernandes & Hardegree-Ullman, R. B., Hardegree-Ullman, K. K., Pascucci, I., et al. 2023, *AJ*, 166, 175
- Fernandes, R. 2022, *pterodactyls: A Tool to Uniformly Search and Vet for Young Transiting Planets In TESS Primary Mission Photometry*, doi:10.5281/zenodo.6667960
- Fernandes, R. B., Mulders, G. D., Pascucci, I., et al. 2022, *AJ*, 164, 78
- Foreman-Mackey, D. 2016, *The Journal of Open Source Software*, 24, doi:10.21105/joss.00024
- Foreman-Mackey, D., Hogg, D. W., Lang, D., & Goodman, J. 2013, *Publications of the Astronomical Society of the Pacific*, 125, 306
- Fulton, B. J., Petigura, E. A., Howard, A. W., et al. 2017, *The Astronomical Journal*, 154, 109
- Furlan, E., Ciardi, D., Everett, M., et al. 2017, *The Astronomical Journal*, 153, 71
- Gagné, J., David, T. J., Mamajek, E. E., et al. 2020, *ApJ*, 903, 96
- Gagné, J., Mamajek, E. E., Malo, L., et al. 2018, *The Astrophysical Journal*, 856, 23
- Gaia Collaboration, Brown, A. G. A., Vallenari, A., et al. 2018, *A&A*, 616, A1
- Gaidos, E., Mann, A., Rizzuto, A., et al. 2017, *Monthly Notices of the Royal Astronomical Society*, 464, 850
- Giacomini, S., Dressing, C. D., Jensen, E. L. N., et al. 2021, *AJ*, 161, 24
- Ginzburg, S., Schlichting, H. E., & Sari, R. 2016, *The Astrophysical Journal*, 825, 29
- Guillochon, J., Ramirez-Ruiz, E., & Lin, D. 2011, *ApJ*, 732, 74
- Gupta, A., & Schlichting, H. E. 2019, *Monthly Notices of the Royal Astronomical Society*, 487, 24
- Gupta, A., & Schlichting, H. E. 2020, *MNRAS*, 493, 792
- Hardegree-Ullman, K. K., Zink, J. K., Christiansen, J. L., et al. 2020, *The Astrophysical Journal Supplement Series*, 247, 28
- Hedges, C. 2021, *Research Notes of the AAS*, 5, 262
- Hippke, M., David, T. J., Mulders, G. D., & Heller, R. 2019, *The Astronomical Journal*, 158, 143
- Hippke, M., & Heller, R. 2019, *Astronomy & Astrophysics*, 623, A39
- Howard, A. W., Marcy, G. W., Bryson, S. T., et al. 2012, *The Astrophysical Journal Supplement Series*, 201, 15

- Howell, S. B., Sobek, C., Haas, M., et al. 2014, *Publications of the Astronomical Society of the Pacific*, 126, 398
- Huber, D., Bryson, S. T., Haas, M. R., et al. 2016, *ApJS*, 224, 2
- Hunter, J. D. 2007, *Computing in Science & Engineering*, 9, 90
- Hut, P. 1981, *A&A*, 99, 126
- Izidoro, A., Raymond, S. N., Morbidelli, A., & Winter, O. C. 2015, *MNRAS*, 453, 3619
- Izidoro, A., Schlichting, H. E., Isella, A., et al. 2022, *ApJL*, 939, L19
- Jackson, B., Barnes, R., & Greenberg, R. 2009, *ApJ*, 698, 1357
- Jones, E., Oliphant, T., Peterson, P., et al. 2001–, *SciPy: Open source scientific tools for Python*, [Online; accessed [jtoday](#)]
- Koskinen, T. T., Lavvas, P., Huang, C., et al. 2022, *ApJ*, 929, 52
- Lee, E. J., & Chiang, E. 2017, *ApJ*, 842, 40
- Lee, E. J., & Connors, N. J. 2021, *ApJ*, 908, 32
- Lopez, E. D., & Fortney, J. J. 2013, *The Astrophysical Journal*, 776, 2
- Mann, A. W., Gaidos, E., Mace, G. N., et al. 2016a, *The Astrophysical Journal*, 818, 46
- Mann, A. W., Newton, E. R., Rizzuto, A. C., et al. 2016b, *The Astronomical Journal*, 152, 61
- Mann, A. W., Vanderburg, A., Rizzuto, A. C., et al. 2017, *The Astronomical Journal*, 155, 4
- Mann, A. W., Vanderburg, A., Rizzuto, A. C., et al. 2018, *AJ*, 155, 4
- Mann, A. W., Johnson, M. C., Vanderburg, A., et al. 2020, *The Astronomical Journal*, 160, 179
- Mann, A. W., Wood, M. L., Schmidt, S. P., et al. 2022, *AJ*, 163, 156
- Martinez, C. F., Cunha, K., Ghezzi, L., & Smith, V. V. 2019, *The Astrophysical Journal*, 875, 29
- Mordasini, C., Alibert, Y., Klahr, H., & Henning, T. 2012, *Astronomy & Astrophysics*, 547, A111
- Mulders, G. D., Pascucci, I., & Apai, D. 2015, *ApJ*, 814, 130
- Mulders, G. D., Pascucci, I., & Apai, D. 2015, *The Astrophysical Journal*, 798, 112
- Mulders, G. D., Pascucci, I., Apai, D., & Ciesla, F. J. 2018, *The Astronomical Journal*, 156, 24
- Mulders, G. D., Pascucci, I., Apai, D., & Ciesla, F. J. 2018, *AJ*, 156, 24
- Nardiello, D., Piotto, G., Deleuil, M., et al. 2020, *Monthly Notices of the Royal Astronomical Society*, 495, 4924
- Newton, E. R., Mann, A. W., Tofflemire, B. M., et al. 2019, *The Astrophysical Journal Letters*, 880, L17
- Newton, E. R., Mann, A. W., Kraus, A. L., et al. 2021, *The Astronomical Journal*, 161, 65
- Offner, S. S. R., Moe, M., Kratter, K. M., et al. 2023, in *Astronomical Society of the Pacific Conference Series*, Vol. 534, *Protostars and Planets VII*, ed. S. Inutsuka, Y. Aikawa, T. Muto, K. Tomida, & M. Tamura, 275
- Owen, J. E., & Schlichting, H. E. 2024, *MNRAS*, 528, 1615
- Owen, J. E., & Wu, Y. 2013, *The Astrophysical Journal*, 775, 105
- . 2017, *The Astrophysical Journal*, 847, 29
- Pascucci, I., Mulders, G. D., & Lopez, E. 2019, *ApJL*, 883, L15
- Pecaut, M. J., & Mamajek, E. E. 2013, *ApJS*, 208, 9
- Perez-Becker, D., & Chiang, E. 2013, *MNRAS*, 433, 2294
- Petigura, E. A., Howard, A. W., & Marcy, G. W. 2013, *Proceedings of the National Academy of Sciences*, 110, 19273
- Petigura, E. A., Marcy, G. W., Winn, J. N., et al. 2018, *The Astronomical Journal*, 155, 89
- Petrovich, C., Deibert, E., & Wu, Y. 2019, *AJ*, 157, 180
- Plavchan, P., Barclay, T., Gagné, J., et al. 2020, *Nature*, 582, 497
- Rasio, F. A., & Ford, E. B. 1996, *Science*, 274, 954
- Rauer, H., Aerts, C., Cabrera, J., et al. 2024, *arXiv e-prints*, [arXiv:2406.05447](#)
- Ricker, G. R., Winn, J. N., Vanderpek, R., et al. 2014, *Journal of Astronomical Telescopes, Instruments, and Systems*, 1, 014003
- Rizzuto, A. C., Mann, A. W., Vanderburg, A., Kraus, A. L., & Covey, K. R. 2017, *The Astronomical Journal*, 154, 224
- Rizzuto, A. C., Vanderburg, A., Mann, A. W., et al. 2018, *The Astronomical Journal*, 156, 195
- Rizzuto, A. C., Newton, E. R., Mann, A. W., et al. 2020, *The Astronomical Journal*, 160, 33
- Rogers, J. G., & Owen, J. E. 2021, *MNRAS*, 503, 1526
- Rogers, J. G., Owen, J. E., & Schlichting, H. E. 2024, *MNRAS*, 529, 2716
- Safsten, E. D., Dawson, R. I., & Wolfgang, A. 2020, *AJ*, 160, 214
- Socrates, A., Katz, B., & Dong, S. 2012, *ArXiv e-prints*, [arXiv:1209.5724](#)
- Teske, J. K., Ciardi, D. R., Howell, S. B., Hirsch, L. A., & Johnson, R. A. 2018, *The Astronomical Journal*, 156, 292
- Thompson, S. E., Coughlin, J. L., Hoffman, K., et al. 2018, *The Astrophysical Journal Supplement Series*, 235, 38
- Vach, S., Zhou, G., Huang, C. X., et al. 2024, *AJ*, 167, 210
- van der Walt, S., Colbert, S. C., & Varoquaux, G. 2011, *Computing in Science & Engineering*, 13, 22

- Van Eylen, V., Agentoft, C., Lundkvist, M., et al. 2018, Monthly Notices of the Royal Astronomical Society, 479, 4786
- Vanderburg, A., Mann, A. W., Rizzuto, A., et al. 2018, The Astronomical Journal, 156, 46
- Venturini, J., Guilera, O. M., Haldemann, J., Ronco, M. P., & Mordasini, C. 2020, A&A, 643, L1
- Weidenschilling, S. J., & Marzari, F. 1996, Nature, 384, 619
- Wu, Y., & Murray, N. 2003, ApJ, 589, 605
- Youdin, A. N. 2011, ApJ, 742, 38
- Zellem, R. T., Pearson, K. A., Blaser, E., et al. 2020, Publications of the Astronomical Society of the Pacific, 132, 054401
- Zhou, G., Wirth, C. P., Huang, C. X., et al. 2022, AJ, 163, 289
- Zink, J. 2019, jonzink/EDI-Vetter: Initial Release, doi:10.5281/zenodo.3585940
- Zink, J. K., Hardegree-Ullman, K. K., Christiansen, J. L., et al. 2020, The Astronomical Journal, 159, 154
- Zuckerman, B. 2019, ApJ, 870, 27

APPENDIX

A. COMPARISON OF `eleanor` VS SPOC

We compare the RMS of `eleanor`, SPOC, and QLP light curves for planet-hosting stars, showing that SPOC light curves generally exhibit the lowest noise levels, making them the most suitable for planet detection. Given their reduced RMS residual scatter relative to `eleanor`, we chose TESS SPOC FFI PDCSAP light curves to improve our sensitivity to small planets in these intrinsically variable data sets.

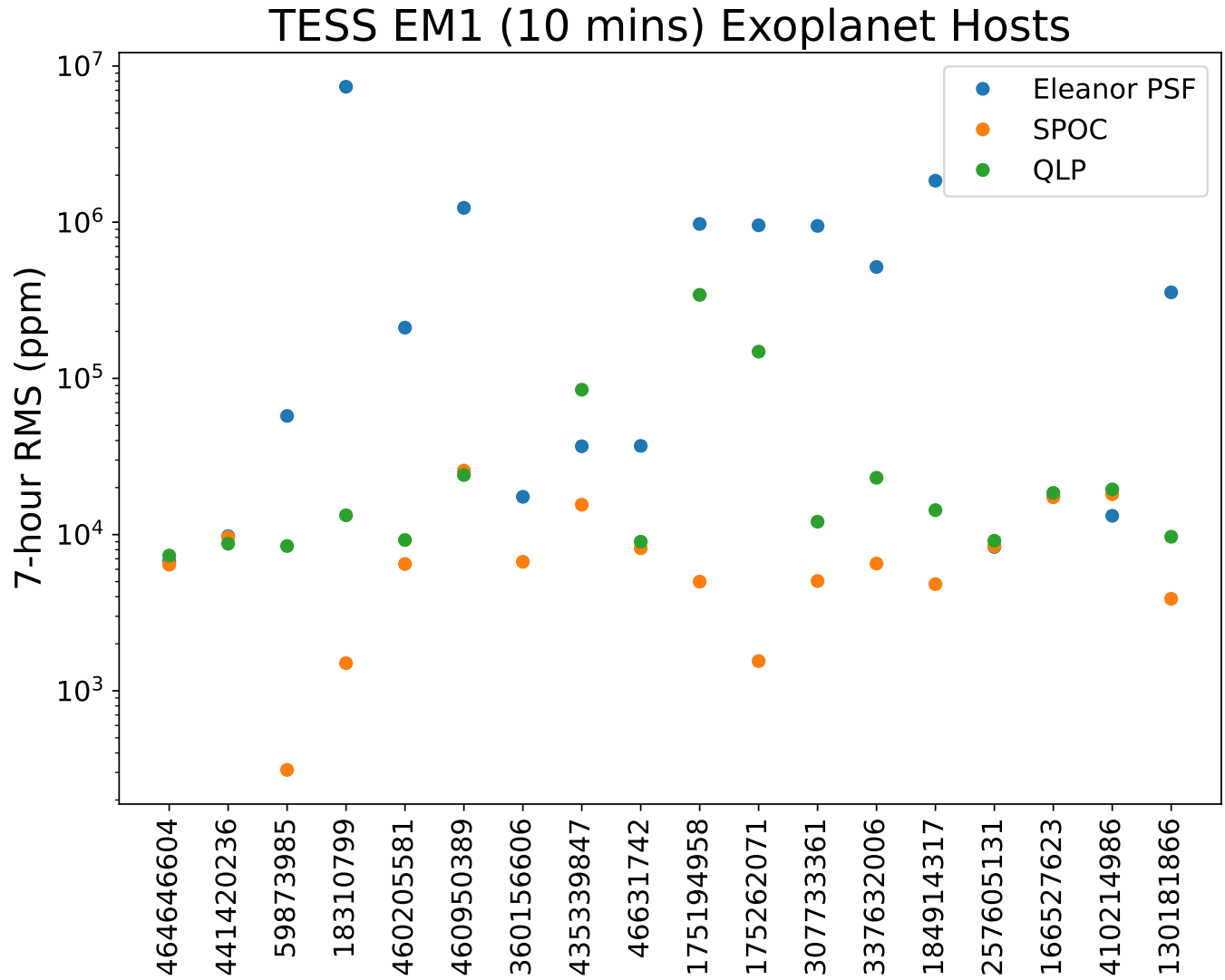


Figure 8. Comparison of RMS of `eleanor`, SPOC and QLP light curves for the planet hosts depicting that, on average, SPOC light curves have the least amount of noise thereby making them ideal for planet searches.

B. SKYE EXCESS METRIC (SEM)

To address cadences with an unusually high number of transit-like detections, we applied a test similar to the “Skye” metric for sectors 27-55, assessing transit-like signals at each cadence. Any cadences where the signal count exceeded 3σ were masked before reprocessing the search to mitigate issues with the light curve.

Skye Excess Metric: TESS EM1 (Year 3)

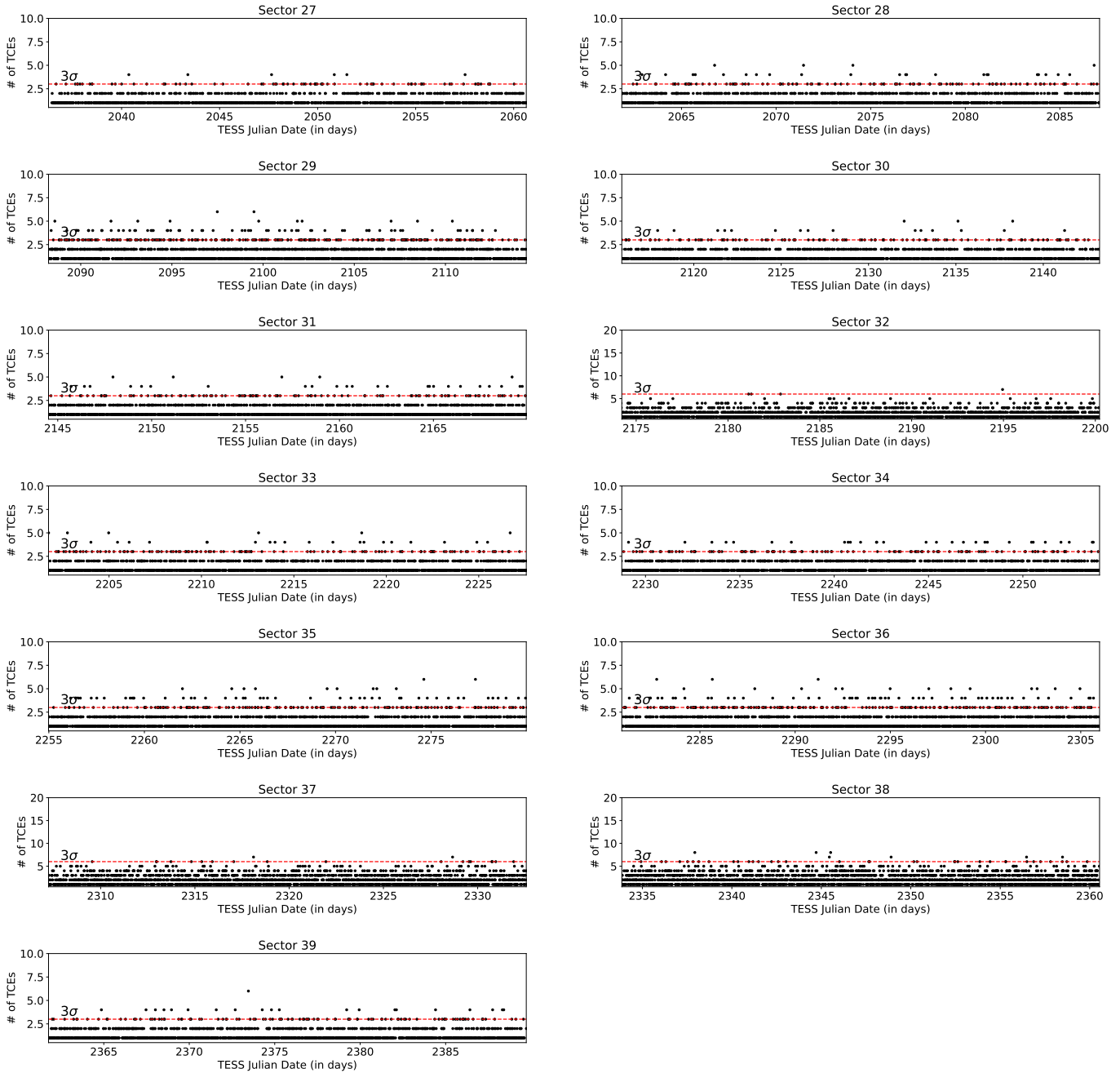


Figure 9. SEM for TESS EM1’s Sectors 27-39

Skye Excess Metric: TESS EM1 (Year 4)

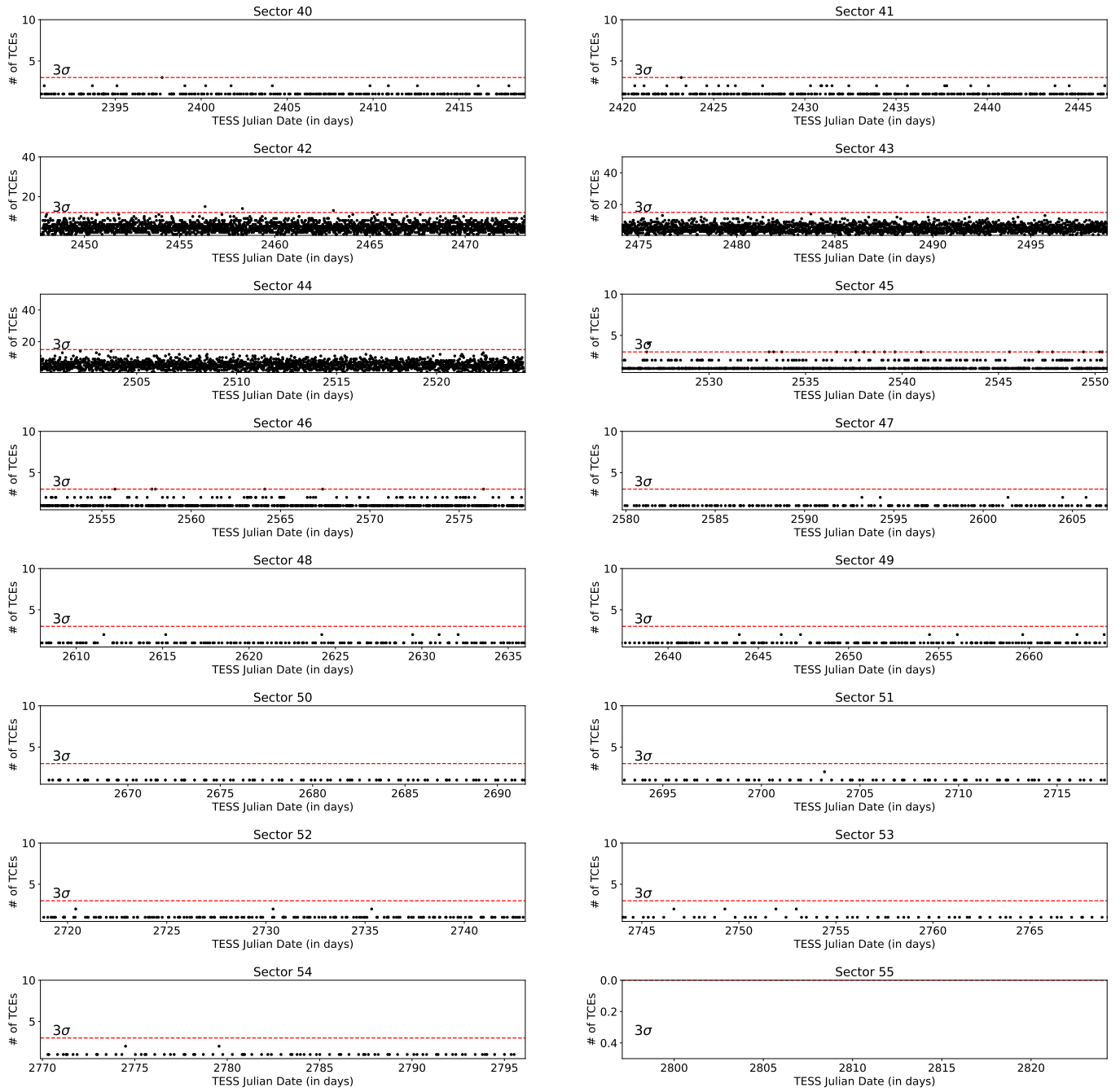


Figure 10. SEM for TESS EM1's Sectors 40-55